Westfälische Wilhelms-Universität Münster
Fachbereich Mathematik und Informatik

Diplomarbeit in Mathematik

Influence of Volume Conduction on Beamformer Source Analysis in the Human Brain

eingereicht von
Stephanie Sillekens

Gutachter:
Prof. Dr. Martin Burger
Priv.-Doz. Dr. Carsten Wolters

Münster, 22.12.2008

Abstract

The effect of volume conduction on brain source reconstruction using beamformer techniques – in particular Synthetic Aperture Magnetometry (SAM) – is investigated.

The sphere model that is commonly used in the analysis of brain activity provides only a very rough representation of the real head geometry, whereas Finite Element (FE) models can model realistic head shapes and head tissue conductivity distributions very accurately. The effect of inaccurate geometry approximation on the beamformer is examined in simulations. We show that the effects are especially large in those regions where the sphere model differs the most from the true head geometry.

It is also common practice to model the head volume to be entirely isotropic. In reality the head has anisotropic compartments as well. We have investigated the effects of skull anisotropy in a realistically shaped FE model. Simulations show that by disregarding the skull anisotropy the depth localization is inaccurate, especially in regions where the skull is relatively thick.

Contents

Acknowledgments

I want to thank

Martin Burger and Carsten Wolters for offering me the chance to write a challenging thesis in an interdisciplinary environment and for always supporting my work.

Olaf Steinsträter for introducing me to the field of beamformer source analysis, for answering and discussing a lot of questions and for supporting me with all kinds of practical computational challenges.

Markus Junghöfer for providing the medical background and for giving me a sense of the applications in neuroscientific research, where accurate source analysis is needed.

Benjamin Lanfer for supplying me with some crucial knowledge on the SCIRun visualization software.

Thomas Dierkes for providing me with software and data needed for the processing and visualization of FE meshes.

my family, Beate, Hans Peter and Thomas Sillekens, for always being there.

Fabian Gigengack, Martin Benning, Andree Große and Ann-Kathrin Bröckelmann for proof-reading my thesis and for making helpful suggestions.

everyone at the Institute of Biomagnetism and Biosignalanalysis for the good working atmosphere.

all my friends and everybody who deserves to be mentioned here.

1 Introduction

The aim of this thesis is the analysis of mathematical methods in the field of electroencephalography (EEG) and magnetoencephalography (MEG), particularly focusing on the prefrontal cortex.
The prefrontal cortex is especially significant in human brain functions and therefore of greatest meaning to human brain research. This is emphasized by the fact that the prefrontal cortex has enlarged enormously compared to other brain regions during evolution. It underwent progressive evolution and is larger in apes than in monkeys and larger in humans than in apes [13]. Therefore it is not surprising that a number of higher brain functions that are particularly assigned to apes–or even entirely to humans–were localized in the prefrontal cortex:
This brain region has been implicated in planning complex cognitive behaviors, personality expression, decision making and moderating correct social behavior. The basic activity of this brain region is considered to be orchestration of thoughts and actions in accordance with internal goals. Thus, the most typical psychological term for functions carried out by the prefrontal cortical (PFC) area are executive control functions.

Moreover, brain source activity in PFC areas has turned out to play a major role in different psychological conditions. It has for example consistently been shown that the amygdala and prefrontal cortical areas play key roles in the control of mood and anxiety. Pathologic anxiety is discussed to be a result of exaggerated amygdala response to stimuli that are not necessarily threatening. Amygdala hyper-reactivity has predominantly been attributed to PFC dysfunction, as PFC regions are responsible for the inhibition of inadequate emotional response. In this context it is now desirable to examine the rapid and transient bottom-up and top-down processes within the human fear circuit.

A further example where PFC activity is majorly involved are schizophrenic disorders. Numerous studies have investigated reduced suppression of sensory gating–an unconscious inhibition of irrelevant stimuli at earliest processing stages–and dysfunctional data processing or impaired attention at the core of the spectrum of schizophrenic disorders. Whether schizophrenic patients reveal disturbances for emotional stimuli is yet to be investigated. Recent MEG studies on affective conditioning in audition and vision have revealed very rapid PFC activity preceding and bottom-up modulating the initial sensory processing. A further investigation of these processes is of high importance to neuro scientific research in order to find out more about reliable neuro biological correlates of pathophysiogical mechanisms as well as endophenotypes.

A common method for the analysis of brain source activity is to apply numerical techniques to EEG or MEG data and thereby estimate the locations of the underlying brain activity. These techniques all require a solution to the forward problem, which in these applications is a calculation of electric/magnetic signals at the EEG/MEG sensors for a known source within a given head volume. The forward solutions strongly depend on the modelling of the head volume. A model that is commonly used is an isotropic multilayer sphere model. The according inverse problem is to compute the brain source from given EEG/MEG measurements.

When interested in PFC activation the usability of the sphere model has turned out to be limited, as the sphere is an inexact approximation of the head shape especially in PFC areas. A promising approach to improving brain source reconstruction is to use realistically shaped Finite Element (FE) head models. On top of a better geometrical representation, FE models give the possibility of modelling anisotropy effects.

The goal of this thesis is to examine the effects of head modelling on the solution of the inverse problem. The inverse procedure that this work will focus on are beamformer techniques and Synthetic Aperture Magnetometry (SAM) in particular.

In order to analyze the 'influence of volume conduction on beamformer source analysis in the human brain', the following topics will be discussed in this thesis:

- We will start with an explanation of some basic neural concepts since they are the basis of the mathematical modelling that allows brain source reconstruction. This explanation will in particular why activity in the human brain is modelled by electric current dipoles.

- The next step is to derive the solution to the forward problem. This will incorporate a derivation of the partial differential equation that describes the forward problem as well as a description of the source model and the head model. The Ritz-Galerkin approach that is used to generate the forward solution will be considered in this context.

- After the introduction of the forward problem the focus lies on the inverse procedure. A detailed derivation of the Linearly Constrained Minimum Variance (LCMV) beamformer is given, followed by a specific description of SAM. An important issue in beamformer source analysis is the estimation of the data covariance matrix which will be further analyzed.

- These theoretical considerations are followed by the actual analysis of the influence of volume conductor modelling on the beamformer source reconstruction. For this purpose synthetic data are produced and analyzed with SAM focusing on geometry effects and anisotropy effects of the head models used. The simulations with their results will be presented and interpreted.

- To complete this thesis, the last chapter will give an outlook on aspects that deserve further consideration in future research.

2 Basic Neural Concepts

The processing of conscious action, sensory perception as well as unconscious reactions include electrical activity in the human brain. Every movement of electric charges causes an electric and a magnetic field. The EEG represents the differences in electric potential resulting from this activity that can be measured at the scalp. The MEG records the magnetic fields at some small distance from the head surface in the range of a few centimeters.

The interpretation of this recorded data in the context of localizing the underlying sources within the brain requires some knowledge of the electrophysiological processes in the human body. This chapter will give a brief overview on the processes that are acting inside the human brain and how they can be recorded by the electroencephalogram. A more detailed description can be found in [40, 44].

2.1 Physiology of the Neuron

The neuron is the structural and functional unit of the nervous system. A typical neuron consists of a cell body (soma) together with two kinds of extensions, the axon and the dendrites. With the dendrites the neuron receives signals from other nerves. The axon that originates at the axon hillock of the soma transmits the signal from the neuron to other nerve-, muscle- or gland cells. In the following this transmission of signals to other neurons will be described. The axon ends in the axon terminals at the synapse and thereby connects to the soma, the dendrites, or the axon of the next neuron (see Figure 2.1). At the synapse information is passed on chemically with the help of neurotransmitters. Within a neuron information is passed electrically. The details of electric information transmission will now be explained.

At the membrane of a living cell a difference in electric potential can be measured. The so-called *resting potential* has a value of -60 to -100 mV depending on the cell type (negative inside the cell). The resting potential is a prerequisite for the ability of neurons to pick up, process, and transmit neural signals. The reason for the potential difference at the cell membrane is an unequal distribution of ions in intracellular and extracellular fluid. The ions that are of interest for the considered processes are potassium (K^+), sodium (Na^+) and chloride (Cl^-). In the resting state the concentration of potassium is much higher inside the cell than outside and vice versa for sodium and chloride. The following phenomena are of importance here:

- The cell membrane is well permeable for K^+ in the resting state. Due to

the large concentration gradient, K^+-ions will diffuse out of the cell, which leads to a change in charge. The membrane is not permeable for protein anions and only very little permeable for Na^+. This diffusion potential will gain until any further diffusion of K^+ is avoided by the gaining potential. Electric and osmotic work now cancel out each other.

- By active transport, which means with energy input, Na^+ is permanently "pumped" out of the cell, while K^+ is pumped in (Na^+-K^+-ATPase). This exchange is electrogenic, which means it can produce charge imbalance across the cell membrane and can also contribute directly to the membrane potential.

- The anions inside the cell are mostly negatively charged proteins.

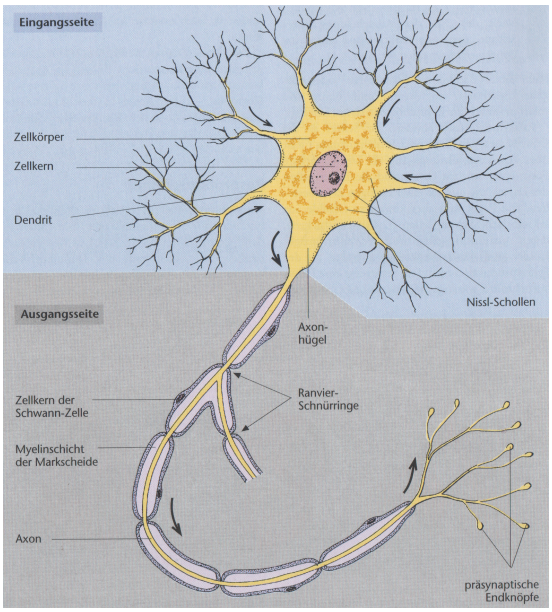

Figure 2.1: Structure of a Neuron (taken from Zalpour [60]). The arrows indicate the direction of the electric current flow. The blue background surrounds the side of the neuron, where information is received: Cell body (Zellkörper), and dendrites (Dendrit). The grey background shows the side where the information is passed on: axon hillock (Axonhügel), axon (Axon) and axon terminals (präsynaptische Endknöpfe).

Two different kinds of information transport will now be described, first the action potential and then the electrotonic conduction.

Action potential The axons of the neurons can have a length of up to 1 m. Without a special mechanism an electric stimulus would quickly reduce to zero

due to the high resistance inside the neuron fibers. Therefore signals are transmitted along the axon as action potentials (AP) as explained in the following: the resting potential of the membrane decreases towards 0 mV (depolarization) and if the stimulus is strong enough to reach the so-called *threshold potential* of -50 to -60 mV an AP can be fired. Reaching the threshold leads to a sudden increase of the Na^+-conductivity and to an inflow of Na^+-ions into the cell via the sodium channels. Thereby the membrane potential quickly breaks down (depolarization of the AP) and currently reaches positive values of up to +30 mV. The conductivity (or rather permeability) for sodium g_{Na^+} decreases again while at the same time the conductivity for potassium g_{K^+} increases, which restores the resting potential of the membrane (repolarisation). The difference in charge between a depolarized and a resting membrane leads to a compensating current along the fibers which depolarizes the adjacent area.

Electrotonic Conduction Dendrites and somata do not have sodium channels, so the transmission of information happens by electrotonic conduction. The electrotonic potential can be described mathematically by the function $\Phi(x) = \Phi_0 e^{-x/\lambda}$, where x is the distance from the application of the electric current and λ is a constant incorporating geometric properties as well as the conductivity of the membrane and the inside of the cell. Φ_0 is the potential at the place of the current application. The sum of all stimuli that are impressed on the dendrites of a neuron and that are conducted to the axon hillock must reach the threshold potential in order to activate an AP that passes the stimulus on.

At the synapse signals are only transmitted in one direction and that is from a presynaptic cell to a postsynaptic cell. This transmission happens chemically via so-called neurotransmitters. A difference is made between excitatory synapses and inhibitory synapses. Acetylcholine as a transmitter leads to an increase of the Na^+-conductivity and thereby to a depolarization. Other transmitters (e.g. glycine) lead to an increase of the conductivity of Cl^- and K^+ resulting in hyperpolarisation of the postsynaptic membrane.

2.2 Functional Histology of the Cerebral Cortex

The brain can anatomically be divided into three major parts, the brainstem, the cerebellum and the cerebrum. The cerebrum consists of a left and a right hemisphere. The inner part, the white matter, is surrounded by a 1.3 to 4.5 mm thick layer of grey matter making up the cerebral cortex (Figure 2.2) and mainly consists of axons. Alltogether, the cerebral cortex can be described as multiply folded layers of tissue. It contains about 10^{10} neurons and a large but unknown number of glia cells that provide support and protection for the neurons.

Inside the cortex there are layers that mostly contain cell bodies next to layers that mostly contain axons. A cut through the cortex would therefore appear to be striped. According to the cell types incorporated six layers are typically

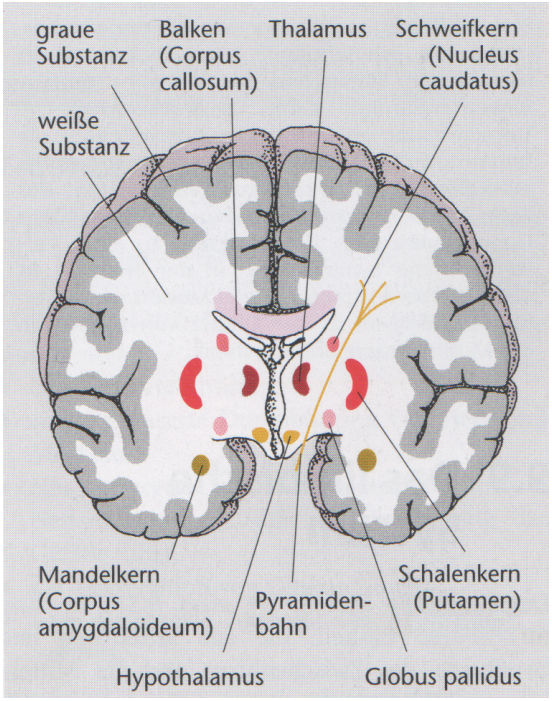

Figure 2.2: Coronal cut through the brain (taken from Zalpour [60]). Left and right hemisphere, grey matter (graue Substanz) and white matter (weiße Substanz).

differentiated:

1. **molecular layer:** This layer mainly consist of fibers but only very few neurons.

2. **external granular layer:** Here small neurons of different shapes can be found which run tangential to the surface.

3. **external pyramidal layer:** This layer mostly contains pyramidal neurons of medium size.

4. **internal granular layer:** Small neurons of different sizes (stellate cells) closely surrounded by fibers running tangentially to the surface.

5. **internal pyramidal layer:** This layer consists of medium size and big pyramidal cells with long dendrites that reach up to the molecular layer. The pyramidal cells lie parallel to each other and perpendicular to the surface of the cortex. This layer is of special importance for the EEG and MEG.

6. **multiform layer:** It is mainly made up from spindle-like pyramidal neurons. The innermost part of this layer fades into the white matter.

Figure 2.3 shows the six layers of the cortex. It shows the neuronal circuits with their afferent and efferent connections.

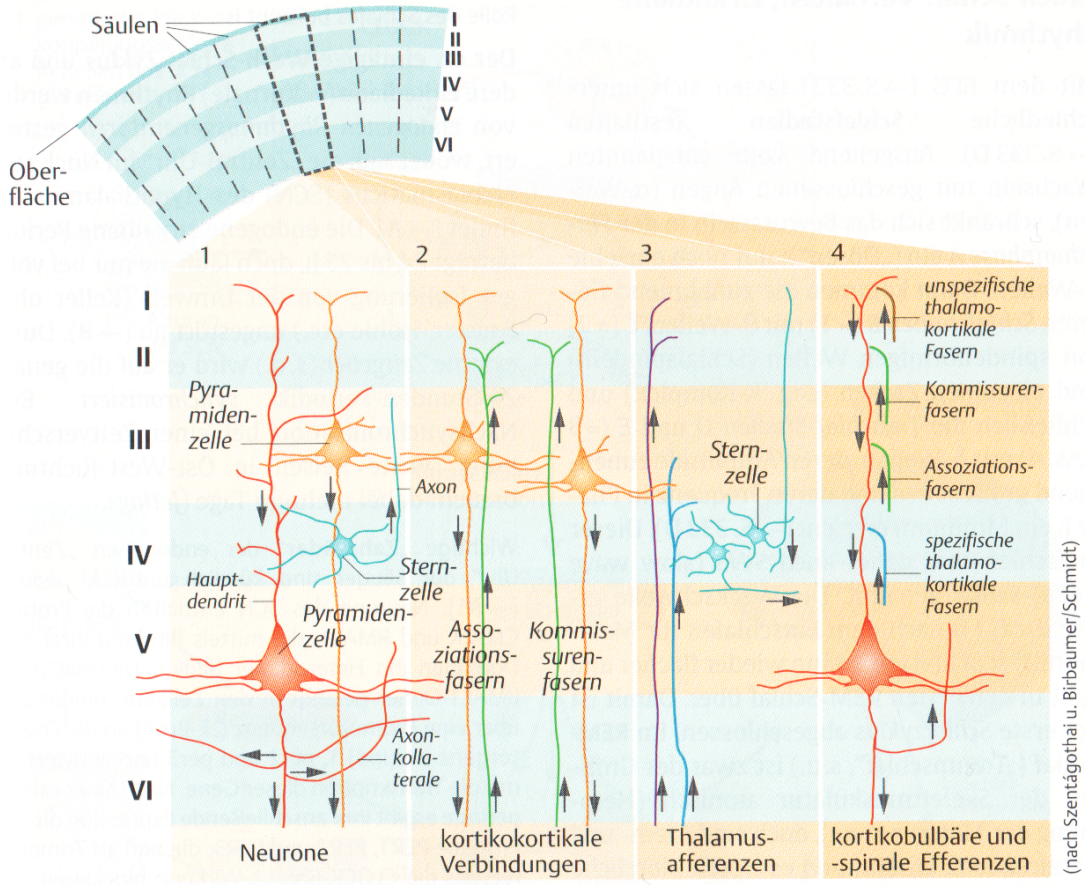

Figure 2.3: The six layers of the cortex: cortical neurons, their circuits with afferent and efferent connections (taken from [44]).

2.3 Electro- and Magnetoencephalogram

EEG: From the skin on the skullcap continuous changes in potential can be derived and recorded as the electroencephalogram. Hans Berger discovered the possibility of recording the electrical activity of the human brain. In the years between 1929 and 1938 he created the foundations for the clinical and experimental use of this method. With the development of highly sensitive detectors cooled with liquid helium (SQUIDS, Superconducting Quantum Interference Devices) the magnetic field was first detected in 1968.

Numerous experiments have shown that the encephalograms essentially result from postsynaptic activity of the cortical neurons rather than from the transmission of these cells' signals (action potentials) or from the activities of cortical glia cells [40]. The fields measured on the outside are mainly generated in the

pyramidal cells inside the 5^{th} layer of the cortex. The AP can physically be modeled as a quadrupole and the postsynaptic potential is modeled as a current dipole. Therefore at the head surface which has a considerable distance from the source, mainly dipole induced fields are measured.

Not a single neuron will account for this measured field but rather a whole brain region with a volume of several mm^3 that is nearly simultaneously activated. A volume of 1 mm^3 contains about 10^5 neurons with about half of them being pyramidal cells. Such a simultaneous activation pattern of large numbers of neurons can be observed over several tens of milliseconds [53].

The recording of the EEG is an internationally used standard routine in neurologic diagnosis. The positions of the electrodes on the head surface and the recording conditions have to a large extent been standardized (international 10-20 system). Modern EEG systems are using up to 128 surface electrodes. The evaluation mainly concentrates on frequency, amplitude, shape, distribution and occurance of the waves recorded in the EEG. Because of a maximum EEG-amplitude of only a few 100 μV it is necessary to amplify the signals by a factor of 10^3 to 10^4 for further analysis.

Due to the fact that spontaneous activity from different areas of the cortex overlaps, the interpretation of the EEG is very complex. It is still possible to differentiate healthy and pathological states and changes in the EEG. Based on the EEG diagnostic conclusions (for example about the awake state, emotional tension, the brain's stage of maturity as well as some diseases) can be drawn. A deeper analysis of the contained frequencies has shown that certain periodic sub signals within a frequency band of 0.5 to 30 Hz and amplitudes between 10 and 150 μV are predominant. The frequency spectrum is usually divided into four frequency bands:

denomination	**frequency**	**amplitude**
δ-waves	$0.5 - 3$ Hz	$100 - 150$ μV
ϑ-waves	$4 - 7$ Hz	$50 - 100$ μV
α-waves	$8 - 13$ Hz	ca. 30 μV
β-waves	$14 - 30$ Hz	ca. 10 μV

Variations in the potential are usually dependent on the state of awakeness. In a healthy adult in a resting state with eyes closed, the α-rhythm is especially predominant in the occipital direction. When opening the eyes or receiving other sensual stimuli the α-waves disappear and β-waves with higher frequency but lower amplitude are observed. Slower waveforms of higher amplitude like the ϑ-waves and δ-waves can only be observed during sleep in an adult (Figure 2.4). As mentioned before there is also a clinical meaning to the EEG. A slowing down and irregularities in the potential curves are symptomatic for diffuse organic brain diseases, after brain traumata or metabolic intoxication (coma). EEG irregularities can also occur due to tumors or medicals (psychotropics). The cease of the EEG is more and more used as a criterion for brain death.

MEG: The magnetoencephalogram (MEG) records the magnetic activity of the brain. The magnetic flux passing through specially shaped, supra conducting measuring coils (magnetometer or gradiometer respectively) is measured by SQUIDS. The field strength lies in a range of 10^{-12} to 10^{-13} Tesla (T) [53]. The magnetic field of the earth has an order of 10^{-4} T. The complexity of the measurements is accordingly high. The measurements are recorded in magnetically shielded chambers in order to eliminate disturbing influences, for example from the terrestrial magnetic field or electric cable. The advantage of the MEG compared to the EEG is an up to ten times higher signal to noise ratio (SNR).

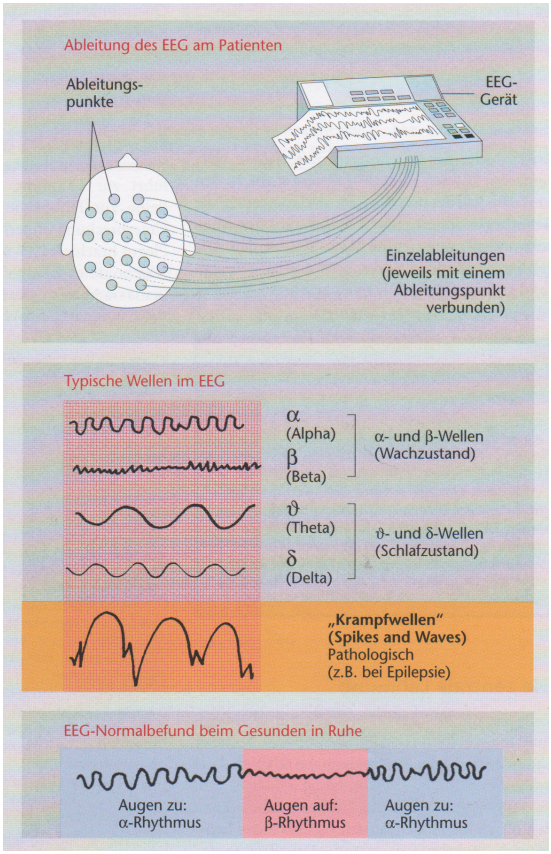

Figure 2.4: Top to bottom: Electric potentials are recorded by head surface electrodes. Typical α-, β-, ϑ-, δ-waves, seizure potentials on orange background. Normal EEG-record of a healthy subject, changing between α- and β-waves. (taken from [60])

2.4 Evoked and Induced Potential

Apart from spontaneous activity in the cortex, variations in the potentials are mainly due to psychological, motor or sensory events. These characteristical potentials usually show only small amplitudes and therefore summation techniques

are necessary to visualize them. Those variations in the electric potentials that are located in the central nervous system as a response to stimulated receptors, to peripheral nerves or other sensoric structures are called evoked potentials (EP). By stimulation of peripheral somatic receptors or neurons, slow positive-negative changes in the potential are registered in the somatosensory areas of the cortex, which are called sensory evoked potentials (SEP). The diagnostic meaning of the measurement of EP lies in testing the proper function of the peripheral sensory and subcortical nervous system. The inverse analysis of the EEG and MEG serves to identify the exact position of the processing of the EPs. Analogously to the SEP, visually evoked potentials (VEP) can be registered. The respective areas of the cortex are shown in Figure 2.5.

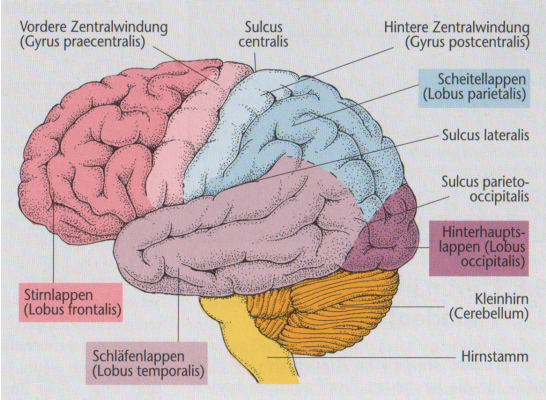

Figure 2.5: Lateral view of the main areas of the cerebral cortex (frontal (Lobus frontalis), temporal (Lobus temporalis), parietal (Lobus parietalis) and occipital(Lobus occipitalis) cortex)(taken from [60]).

An important property of EPs is that they are time locked to the stimulus. This allows the averaging of recorded data trials in order to increase the SNR, which is crucial for a number of inverse methods.

In this context induced potentials should also be mentioned. These potentials underly brain activity that is not time locked to a particular stimulus. Therefore averaging across trials is not possible as it might cancel out the signal. For the analysis of induced potentials the inverse method must be chosen very carefully. The beamformer techniques introduced later in this thesis are one possible choice because they do not only operate on averaged data but on single trials as well.

3 The Forward Problem

In order to solve the inverse problem it is necessary to find a solution to the forward problem first. In the case of EEG/MEG source reconstruction, solving the forward problem means the following: For a given source location in the brain with known source strength and direction, we need to find the electric/magnetic potentials that would be measured at the sensor locations.

To fulfill this task, some crucial steps are necessary. These include expressing the behaviour of electric currents within biological tissue mathematically, which can be done with the help of the Maxwell Equations of electrodynamics. Further a model for the electric sources in the human brain must be introduced, which will be discussed in Section 3.3. Another focus of this chapter will be to find a volume conductor model for the human head that takes specific anatomical properties of the individual subject into account. This will be done using finite element models.

3.1 The Maxwell Equations

In order to find the forward solution to the problem introduced above, the behaviour of electric and magnetic fields within the head volume must be described mathematically. This is done by the Maxwell Equations of electrodynamics (see e.g. Nolting [25]) using the following notations. $\mathbf{E}$ and $\mathbf{D}$ denote the electric field and electric displacement respectively, ρ the electric free charge density, ϵ the electric permittivity and $\mathbf{j}$ the electric current density. By μ the magnetic permeability is denoted, by $\mathbf{H}$ the magnetic field and by and $\mathbf{B}$ the magnetic induction.

In this application the low frequency band (frequencies below 1000 Hz) is considered. Therefore the capacitative component of tissue impedance, the inductive effect and the electromagnetic propagation effect and thus the temporal derivatives can be neglected in the Maxwell Equations [39] resulting in the quasi-static Maxwell Equations

$$\nabla \cdot \mathbf{D} = \rho$$
$$\nabla \times \mathbf{E} = 0$$
$$\nabla \times \mathbf{B} = \mu \mathbf{j} \tag{3.1}$$
$$\nabla \cdot \mathbf{B} = 0 \tag{3.2}$$

with material equations

$$\mathbf{D} = \epsilon \mathbf{E} \tag{3.3}$$
$$\mathbf{B} = \mu \mathbf{H}. \tag{3.4}$$

It is generally assumed that μ is constant over the whole head volume Ω and equal to the magnetic permeability of vacuum [31]. The electric field can then be described as the negative gradient of a scalar potential Φ:

$$\mathbf{E} = -\nabla \Phi. \tag{3.5}$$

In bioelectromagnetism the current density is commonly divided into the so-called *primary* or impressed current $\mathbf{j}^p$ and the *secondary* or return currents $\boldsymbol{\sigma}\mathbf{E}$

$$\mathbf{j} = \mathbf{j}^p + \boldsymbol{\sigma}\mathbf{E} \tag{3.6}$$

with $\boldsymbol{\sigma}$ denoting the 3×3 symmetric, positive definite conductivity tensor describing the tissue conductivity in all different directions.

3.2 The Poisson Equation of the Electric Forward Problem

The aim is to find the potential Φ to a given primary current $\mathbf{j}^p$. The formulae above must therefore be rearranged to a partial differential equation that can be solved for Φ using some techniques discussed later on in this chapter. Applying Divergence to (3.1) and noting that μ is a scalar value and that the vector identity $\nabla \cdot \nabla \times \mathbf{B} = 0$ holds, we receive

$$\nabla \cdot \nabla \times \mathbf{B} = \nabla \cdot \mu \mathbf{j} = \mu \nabla \cdot \mathbf{j} = 0. \tag{3.7}$$

Substituting (3.5) and (3.6) this can further be rewritten to

$$\begin{aligned} 0 &= \nabla \cdot \mathbf{j} \\ &= \nabla \cdot (\mathbf{j}^p + \boldsymbol{\sigma}\mathbf{E}) \\ &= \nabla \cdot \mathbf{j}^p + \nabla \cdot \boldsymbol{\sigma}(-\nabla \Phi) \\ &= \nabla \cdot \mathbf{j}^p - \nabla \cdot (\boldsymbol{\sigma} \nabla \Phi), \end{aligned} \tag{3.8}$$

resulting in the Poisson equation

$$\nabla \cdot (\boldsymbol{\sigma} \nabla \Phi) = \nabla \cdot \mathbf{j}^p = J^p \text{ in } \Omega. \tag{3.9}$$

The Poisson equation represents the distribution of the electric potential Φ over the head volume Ω due to primary current $\mathbf{j}^p$ in the cortex of the human brain. At the head surface $\Gamma = \partial\Omega$ homogeneous Neumann boundary conditions hold, which can be expressed as

$$\langle \boldsymbol{\sigma} \nabla \Phi, \mathbf{n} \rangle = 0 \text{ on } \Gamma, \tag{3.10}$$

where $\mathbf{n}$ is the unit surface normal and a reference electrode with given potential $\Phi(\mathbf{q}_{ref}) = 0$ is assumed. The continuity of the current density across surfaces between regions of different conductivities $\boldsymbol{\sigma}_1$ and $\boldsymbol{\sigma}_2$ can be expressed by the boundary condition

$$\langle \boldsymbol{\sigma}_1 \nabla \Phi_1, \mathbf{n} \rangle \mid_{\text{at surface}} = \langle \boldsymbol{\sigma}_2 \nabla \Phi_2, \mathbf{n} \rangle \mid_{\text{at surface}} . \tag{3.11}$$

Furthermore a compatibility condition must be respected, which means that according to Gauss' theorem

$$\int_\Omega J^p d\Omega = 0 \tag{3.12}$$

must hold (see for example [5, 16, 59]).

3.3 The Primary Currents

A crucial point that deserves discussion when considering the Poisson equation (3.9) is modelling the primary current J^p on the right-hand side.

In reality the primary currents are movements of ions within the dendrites of the large Pyramidal cells of activated regions of the cortex. As described in [55] stimulus-induced activation of a large number of excitatory synapses of a whole pattern of neurons leads to negative current monopoles under the brain surface and to positive monopoles quite closely underneath [26, 2].

It is shown in [27] that already at distances as small as the activated area only the dipolar moment of the source term is visible. Therefore the mathematical dipole is a commonly accepted model in the field of bioelectromagnetism [12]. A dipole at position $\mathbf{q}_0 \in \mathbb{R}^3$ is defined as

$$\mathbf{j}^p_{dip}(\mathbf{q}) := \mathbf{m}\delta(\mathbf{q} - \mathbf{q}_0), \tag{3.13}$$

where $\mathbf{m} \in \mathbb{R}^3$ represents the dipole moment and δ is the Dirac δ distribution with the properties

$$\int_\Omega \delta(\mathbf{q} - \mathbf{q}_0) d\mathbf{q} = \begin{cases} 1, & \text{if } \mathbf{q}_0 \in \Omega \\ 0, & \text{else} \end{cases} \tag{3.14}$$

$$\delta(\mathbf{q} - \mathbf{q}_0) = 0 \qquad \forall \mathbf{q} \neq \mathbf{q}_0 \tag{3.15}$$

(see also Nolting [25]). Using the mathematical dipole as a source model for the primary current, the right-hand side of the Poisson equation (3.9) can be written as

$$J^p_{dip}(\mathbf{q}) = \nabla \cdot \mathbf{j}^p_{dip}(\mathbf{q}) = \nabla \cdot \mathbf{m}\delta(\mathbf{q} - \mathbf{q}_0). \tag{3.16}$$

Another approach to modelling the primary current is to use a direct approach. The so called *blurred dipole* as introduced by Buchner et al. [8] introduces a smoother current term compared to the mathematical dipole. The blurred dipole does not compress the activation of a small cortex region to a single point but rather distributes it over a small area, which probably represents the reality better. According to [8, 55] the dipole moment is here approximated by a whole collection of closely neighboured sources and sinks.

3.4 The Subtraction Approach

The so called subtraction method [59] provides a way of dealing with strong singularities of the source model. The basic idea is to split up the total potential Φ into a singularity potential Φ^∞ and a correction potential Φ^{corr}

$$\Phi = \Phi^\infty + \Phi^{corr}. \tag{3.17}$$

Splitting the potential into these parts is motivated as follows. It is assumed that for the source position $\mathbf{q}_0 \in \mathbb{R}^3$ there exists a non-empty region $\Omega^\infty \subset \Omega$ of constant homogeneous conductivity $\boldsymbol{\sigma}^\infty$ (the homogeneous conductivity of the grey matter) with $\mathbf{q}_0 \in \Omega^\infty \setminus \partial\Omega^\infty$.

For the subtraction method the conductivity $\boldsymbol{\sigma}$ is split into two parts

$$\boldsymbol{\sigma} = \boldsymbol{\sigma}^\infty + \boldsymbol{\sigma}^{corr}, \tag{3.18}$$

so that $\boldsymbol{\sigma}^\infty$ is constant over the whole volume conductor Ω and $\boldsymbol{\sigma}^{corr}$ is zero in the subregion Ω^∞: $\boldsymbol{\sigma}^{corr}(\mathbf{q}) = 0, \forall \mathbf{q} \in \Omega^\infty$. The singularity potential Φ^∞ is now defined as the forward solution for a dipole in the unbounded homogeneous conductor with constant conductivity $\boldsymbol{\sigma}^\infty = \sigma^\infty \mathbf{I}$ (this expression is valid for a scalar conductivity value $\sigma^\infty \in \mathbb{R}^+$ in the isotropic case). An analytical solution to the Poisson equation

$$\Delta\Phi^\infty = J^p/\sigma^\infty \tag{3.19}$$

is then given by ([39])

$$\Phi^\infty(\mathbf{q}) = \frac{1}{4\pi\sigma^\infty} \int_\Omega \frac{J^p(\mathbf{q}')}{|\mathbf{q} - \mathbf{q}'|} d\mathbf{q}' \tag{3.20}$$

In the case where the mathematical dipole (3.16) is used as a source model, using the vector identity

$$\nabla' \cdot (\mathbf{j}^p(\mathbf{q}')|\mathbf{q} - \mathbf{q}'|^{-1}) = |\mathbf{q} - \mathbf{q}'|^{-1} \nabla' \cdot \mathbf{j}^p(\mathbf{q}') + \mathbf{j}^p(\mathbf{q}') \cdot \nabla' |\mathbf{q} - \mathbf{q}'|^{-1} \tag{3.21}$$

and applying Gauss' theorem, (3.20) can be written as (see [39])

$$\Phi^{\infty}_{\text{math}}(\mathbf{q}) = \frac{1}{4\pi\sigma^{\infty}} \frac{\langle \mathbf{m}, (\mathbf{q} - \mathbf{q}_0) \rangle}{|\mathbf{q} - \mathbf{q}_0|^3}. \tag{3.22}$$

The next step is now to find the correction potential. By subtracting (3.19) from (3.9) we get (see [59])

$$\nabla \cdot (\boldsymbol{\sigma} \nabla \Phi^{corr}) = \nabla \cdot ((\boldsymbol{\sigma} - \boldsymbol{\sigma}^{\infty}) \nabla \Phi^{\infty}) \text{ in } \Omega \tag{3.23}$$

with inhomogeneous Neumann boundary conditions

$$\boldsymbol{\sigma} \frac{\partial \Phi^{corr}}{\partial \mathbf{n}}\Big|_{\Gamma} = -\boldsymbol{\sigma} \frac{\partial \Phi^{\infty}}{\partial \mathbf{n}}\Big|_{\Gamma}. \tag{3.24}$$

Once this equation is solved towards Φ^{corr} the potential Φ can be calculated with the help of (3.17) and (3.22).

3.5 The Venant Approach

The Venant approach provides a method to solve the Poisson equation (3.9) with boundary conditions (3.10) and a fixed reference potential in the case where a blurred dipole is used as a source model on the right-hand side of the Poisson equation. The Venant approach proposed by Buchner et al. [8] is dependent on the FE mesh and will therefore be discussed in Section 3.6

3.6 Finite Element Formulation

The task of simulating fields in realistically shaped volume conductors requires numerical methods. The method of choice in this thesis is the Finite Element (FE) method. It has shown to be appropriate in this context because it can treat geometries of arbitrary shapes and conductivities. This includes isotropic material properties as well as anisotropic ones. The FE method is used by different research groups within the community of bioelectromagnetism (see e.g. [4, 8, 19, 24, 28, 32, 33, 34, 37, 48, 57]).

3.6.1 Variational Expression of the Forward Problem

For the mathematical dipole and the subtraction approach, the variational formulation was derived by Wolters et al. in [59]. Solvability and uniqueness of the correction potential was proven in their study. However, this thesis is mainly concerned with the Venant approach (see [8]), especially because of its computational efficiency.

In the following the goal is to solve the Poisson equation (3.9) with boundary conditions (3.10) and a fixed reference potential in combination with a smoothly

distributed source model using the FE method. In order to fulfill this task a weak formulation of the Poisson equation is needed. A weak formulation is generally gained by multiplying with a test function, integrating and then applying integration by parts. In the present application this results in the variational equation (see [55])

$$a(\Phi, \mathrm{v}) = l(\mathrm{v}) \tag{3.25}$$

with the bilinear form $a(\cdot,\cdot)$ and the functional $l(\cdot)$ defined as

$$a(\Phi, \mathrm{v}) := \int_\Omega \nabla\Phi \cdot (\boldsymbol{\sigma}\nabla \mathrm{v}) d\Omega \tag{3.26}$$

$$l(\mathrm{v}) = \langle l, \mathrm{v}\rangle := -\int_\Omega J^p \mathrm{v} d\Omega. \tag{3.27}$$

In the following it is assumed that $\Phi \in H^1(\Omega)$, with $H^1(\Omega)$ being a Sobolev space over Ω (for definition see for example [5] or [9]) and that J^p is sufficiently smooth (let us assume $J^p \in L^2(\Omega)$). A further definition that is needed is

$$H^1_U := \left\{ \mathrm{v} \in H^1(\Omega) \mid \int_\Omega \mathrm{v} d\Omega = 0 \right\}. \tag{3.28}$$

In order to apply the following theorems to $a(\cdot,\cdot)$ and $l(\cdot)$, certain properties have to be verified, which has been done by Wolters in [54, 59]. For $a(\cdot,\cdot)$ continuity in $H^1(\Omega) \times H^1(\Omega)$ and ellipticity in H^1_U were shown using Cauchy-Schwarz's inequality and a variant of Friedrich's inequality respectively. It was also shown that $l(\cdot)$ is bounded in $H^1(\Omega)$, so that $l \in (H^1_U)'$. For the following theorem we define

$$\mathbb{V} := H^1_U(\Omega) \text{ and } H := H^1(\Omega). \tag{3.29}$$

Theorem 3.6.1 (Existence and Uniqueness)**.** *Let Ω be a bounded domain, Γ a sufficiently smooth boundary and $\boldsymbol{\sigma} \in L^\infty(\Omega)$. Let $\mathbb{V}$ be a closed convex set in a Hilbert space H and $a : \mathbb{V}\times\mathbb{V} \to \mathbb{R}$ an elliptic bilinear form. Then the variational problem*

$$Var(\mathrm{v}) := \frac{1}{2} a(\mathrm{v}, \mathrm{v}) - \langle l, \mathrm{v}\rangle \to min! \tag{3.30}$$

has one and only one solution in $\mathbb{V}$ for each $l \in \mathbb{V}'$. In particular, the solution Φ is characterized through

$$a(\Phi, \mathrm{v}) = \langle l, \mathrm{v}\rangle \qquad \forall \mathrm{v} \in \mathbb{V}. \tag{3.31}$$

Because of the compatibility condition (3.12)*,* (3.31) *is also valid for $\mathrm{v} = const$ and therefore $\forall \mathrm{v} \in H$.*

Proof. Theorem of Lax-Milgram, Characterisation theorem, see for example [5, 54, 59]. □

Theorem 3.6.2. *If the conductivities are discontinuous, the solution* Φ *to equation* (3.30) *is generally not a classical solution. That is* $\Phi \notin C^2(\Omega) \cap C^1(\overline{\Omega})$*, but it has discontinuous derivatives on each boundary with jumping conductivity. Only the tangential derivatives along those boundaries can be continuous.*

Proof. Hackbusch [16]. □

3.6.2 Ritz-Galerkin Approach

The basic idea of the FE method is to discretize the head domain (source space) and to approximate the potential Φ as a linear combination of given basis functions that are defined on the discretized source space [9]. This process will now be described in more detail.

The task that is considered here is to find a $\Phi \in \mathbb{V}$ satisfying

$$a(\Phi, \mathrm{v}) = \langle l, \mathrm{v} \rangle \qquad \forall \mathrm{v} \in \mathbb{V}. \tag{3.32}$$

In order to find a numerical solution of this problem, $\mathbb{V}$ is discretised by choosing a finite dimensional subspace $\mathbb{V}_h \subset \mathbb{V}$ with dimension $\dim \mathbb{V}_h = N_h$ and with basis functions $\psi_1, ..., \psi_{N_h}$ as described in [55, 59]. The average mesh size is denoted by subscript h and $N_h = O(h^{-3})$ is the number of unknowns. An approximation of Φ is now generated using a Ritz-Galerkin approach, which means that in analogy to (3.32) we are searching for a $\Phi_h \in \mathbb{V}_h$ so that

$$a(\Phi_h, \mathrm{v}_h) = \langle l, \mathrm{v}_h \rangle \qquad \forall \mathrm{v}_h \in \mathbb{V}_h. \tag{3.33}$$

For any coefficient vector $\tilde{\Phi}_h = (\tilde{\Phi}_h^{[1]}, ..., \tilde{\Phi}_h^{[N_h]}) \in \mathbb{R}^{N_h}$ the mapping $\mathbf{P} : \mathbb{R}^{N_h} \to \mathbb{V}_h$ is defined as

$$\Phi_h(\mathbf{q}) = \mathbf{P}\tilde{\Phi}_h := \sum_{i=1}^{N_h} \tilde{\Phi}_h^{[i]} \psi_i(\mathbf{q}). \tag{3.34}$$

Using (3.34) the discrete variational problem (3.33) can be interpreted as a linear equation system

$$\mathbf{K}_h \tilde{\Phi}_h = \tilde{\mathbf{j}}_h \tag{3.35}$$

with

$$\mathbf{K}_h^{[ij]} := a(\psi_j, \psi_i) \qquad \forall i, j : 1 \le i, j \le N_h \tag{3.36}$$

$$\tilde{\mathbf{j}}_h^{[i]} := l(\psi_i) \qquad \forall i : 1 \le i \le N_h. \tag{3.37}$$

From the ellipticity of the bilinear form $a(\cdot,\cdot)$ it can be followed that the matrix $\mathbf{K}_h$ is symmetric positive definite. As the discretisation gets finer, the Ritz-Galerkin approximation converges towards the analytical solution, which is stated by the following theorem.

Theorem 3.6.3 (Convergence)**.** *Let $\mathbb{V}_h^i \subset \mathbb{V}$ $(i \in \mathbb{N})$ be a sequence of subspaces with*

$$\lim_{i\to\infty} d(\Phi, \mathbb{V}_h^i) = 0 \qquad \forall \Phi \in \mathbb{V}, \tag{3.38}$$

for the distance function d equal to $d(\Phi, \mathbb{V}_h^i) = \inf_{w\in\mathbb{V}_h^i} \|\Phi - w\|_{\mathbb{V}}$. Let $a(\cdot,\cdot)$ be a continuous and $\mathbb{V}$-elliptic bilinear form. The Ritz-Galerkin approximation $\tilde{\Phi}_h^i \in \mathbb{V}_h^i$ is then converging against Φ:

$$\|\Phi - \tilde{\Phi}_h^i\|_{\mathbb{V}} \xrightarrow{i\to\infty} 0. \tag{3.39}$$

A sufficient condition for (3.38) *is*

$$\mathbb{V}_h^1 \subset \mathbb{V}_h^2 \subset ... \subset \mathbb{V}, \ \bigcup_{i=1}^{\infty} \mathbb{V}_h^i \text{ dense in } \mathbb{V}. \tag{3.40}$$

Proof. Hackbusch [16]. □

As described by Wolters [55] the head domain Ω is for the present application decomposed into finite elements. The subspace $\mathbb{V}_h \subset \mathbb{V}$ could for example be chosen as the subspace of piecewise linear functions

$$\mathbb{V}_h := \{\Phi_h \in C^0(\overline{\Omega}) \mid \Phi_h \text{ linear on each finite element}\}. \tag{3.41}$$

A basis is then given by the Lagrange FE functions with $\psi_i(\mathbf{q}_j) = \delta_{ij} (1 \le i, j \le N_h)$ where $\mathbf{q}_j$ represents the j^{th} FE vertex and the dimension $N_h = \dim \mathbb{V}_h$ is equal to the number of vertices.

3.6.3 The Blurred Dipole Model

The blurred dipole at a position $\mathbf{q}_l$ (not necessarily a FE node) is represented by a monopole source vector $\tilde{\mathbf{j}}_l \in \mathbb{R}^K$ with entries $\tilde{\mathbf{j}}_l^{[k]}$ that are calculated for all $k \in \{1, ..., K\}$ FE nodes $\mathbf{q}_k$ that are neighbouring the FE node that is closest to the position $\mathbf{q}_l$. The monopole sources are determined to approximate the moment $\mathbf{m}_l$ of a mathematical dipole at $\mathbf{q}_l$ as well as possible but still incorporate the smoothness of a distributed source. The calculation of the $\tilde{\mathbf{j}}_l^{[k]}$ will be described in the following.

The basic relation

$$\mathbf{T}_l = \int_{\Omega} (\mathbf{q} - \mathbf{q}_l) J^p d\mathbf{q} \tag{3.42}$$

for a blurred dipole moment $\mathbf{T}_l \in \mathbb{R}^3$ has been pointed out by Schönen et al. [42] and Nolting [25]. In our application only discrete sources on the K neighbouring nodes of $\mathbf{q}_l$ are considered. So the above equation can be rewritten to

$$\mathbf{T}_l = \sum_{k=1}^{K} \Delta\mathbf{q}_{kl} \tilde{\mathbf{j}}_l^{[k]} \tag{3.43}$$

with $\Delta\mathbf{q}_{kl} := (\mathbf{q}_k - \mathbf{q}_l)$ being the vector from FE node $\mathbf{q}_k$ to the dipole position $\mathbf{q}_l$.

An expression for (3.43) using higher moments has been introduced by Rienäcker et al. [34]. The dipole moments at location $\mathbf{q}_l$ in Cartesian direction r ($r = 1, 2, 3$) with orders $n \in \mathbb{N}$ are denoted by the vector $\bar{\mathbf{T}}_l^r \in \mathbb{R}^{n_0+1}$ ($n_0 \in \mathbb{N}$ is usually chosen as 1 or 2) with

$$(\bar{\mathbf{T}}_l^r)^{[n]} = (\bar{\mathbf{T}}_l^r)^{[n]}(\tilde{\mathbf{j}}_l) := \sum_{k=1}^{K} (\Delta\bar{\mathbf{q}}_{kl}^r)^{[n]} \tilde{\mathbf{j}}_l^{[k]} \qquad \forall n = 0, ..., n_0. \tag{3.44}$$

The bar over the $\Delta\mathbf{q}_{kl}^r$ indicates that a scaling by a reference length a_{ref} has been performed so that

$$\Delta\bar{\mathbf{q}}_{kl}^r = \Delta\mathbf{q}_{kl}^r / a_{ref} < 1 \tag{3.45}$$

is dimensionless and the physical dimension of the resulting scaled n^{th} order moment $(\bar{\mathbf{T}}_l^r)^{[n]}$ is that of a current [8, 55, 56]. Furthermore some definitions are made:

$$\bar{\mathbf{X}}_l^r \in \mathbb{R}^{(n_0+1)\times K} \text{ with } (\bar{\mathbf{X}}_l^r)^{[nk]} := (\Delta\bar{\mathbf{q}}_{kl}^r)^n \tag{3.46}$$

$$\bar{\mathbf{m}}_l^r \in \mathbb{R}^{n_0+1} \text{ with } (\bar{\mathbf{m}}_l^r)^{[n]} := \mathbf{m}_l^r \left(\frac{1}{2a_{ref}}\right)^n (1 - (-1)^n) \tag{3.47}$$

$$\bar{\mathbf{W}}_l^r \in \mathbb{R}^{K\times K} \text{ with } \bar{\mathbf{W}}_l^r := DIAG((\Delta\bar{\mathbf{q}}_{1l}^r)^s, ..., (\Delta\bar{\mathbf{q}}_{Kl}^r)^s) \tag{3.48}$$

with $s = 0$ or $s = 1$ [56].

The problem of approximating the dipole moment as well as possible with a smoothly distributed source load can now be expressed by the minimization problem

$$F_\lambda(\tilde{\mathbf{j}}_l) = \|\bar{\mathbf{m}}_l^r - \bar{\mathbf{T}}_l^r\|_2^2 + \lambda\|\bar{\mathbf{W}}_l^r\tilde{\mathbf{j}}_l\|_2^2 = \|\bar{\mathbf{m}}_l^r - \bar{\mathbf{X}}_l^r\tilde{\mathbf{j}}_l\|_2^2 + \lambda\|\bar{\mathbf{W}}_l^r\tilde{\mathbf{j}}_l\|_2^2 \to \min. \tag{3.49}$$

As described by Wolters in [55] the first part of the functional F_λ proposes a minimal difference between the resultant higher moments of the blurred dipole and those of the mathematical dipole, while the regularisation with parameter λ in the second part determines the smoothness of the monopole distribution and enables a unique minimum for F_λ. A solution to this minimization is then given by

$$\sum_{r=1}^{3} \left\{ (\bar{\mathbf{X}}_l^r)^T \bar{\mathbf{X}}_l^r + \lambda (\bar{\mathbf{W}}_l^r)^T \bar{\mathbf{W}}_l^r \right\} \tilde{\mathbf{j}}_l = \sum_{r=1}^{3} \left\{ (\bar{\mathbf{X}}_l^r)^T \bar{\mathbf{m}}_l^r \right\}. \tag{3.50}$$

3.6.4 The Direct Approach Exploiting the Blurred Dipole Model

After the monopole loads for a blurred dipole have been derived in Section 3.6.3 for a local region around the source position (only the neighbouring FE nodes), this model has to be transformed into a global model including the source loads at all FE nodes. For a source location $\mathbf{q}_l$ this yields the vector $\tilde{\mathbf{j}}_h^{[i]} \in \mathbb{R}^{N_h}$ with

$$\tilde{\mathbf{j}}_h^{[i]} := \begin{cases} \tilde{\mathbf{j}}_l^{[k]} \text{ if } \exists k \in \{1, ..., K\} : i = GLOB(k) \\ 0 \text{ otherwise,} \end{cases} \tag{3.51}$$

where the function $GLOB$ determines the global index i to each of the local indices k.

The linear equation system to the variational equation (3.33) thus concludes to

$$\mathbf{K}_h \tilde{\Phi}_h = \tilde{\mathbf{j}}_h \tag{3.52}$$

with K_h defined as in (3.36) and $\tilde{\mathbf{j}}_h$ defined as in (3.51). The forward solution $\tilde{\Phi}_h$ is now obtained by solving this linear equation system.

3.6.5 Generating the Forward Solution Using Transfer Matrices

Many approaches for solving the inverse problem require the forward solution to a large number of dipole positions and orientations. In practice this means that whenever the right-hand side of (3.52) is changed, a whole new linear equation system must be solved from scratch. This results in high computational costs.

Wolters et al. describe how these computational costs can be reduced by introducing the concept of transfer matrices in [58]. Assuming that the positions of the s_{eeg} EEG electrodes directly correspond to the FE nodes at the surface of the head model, it is straightforward to define a restriction matrix $\mathbf{R} \in \mathbb{R}^{(s_{eeg}-1) \times N_h}$ with only one non-zero entry (with value 1) per row that maps the potential vector $\tilde{\Phi}_h$ to the $(s_{eeg} - 1)$ non-reference EEG electrodes:

$$\tilde{\Phi}_{eeg} := \mathbf{R} \tilde{\Phi}_h. \tag{3.53}$$

Defining the so-called transfer matrix $\mathbf{T}$ for the EEG as

$$\mathbf{T} := \mathbf{R} \mathbf{K}_h^{-1} \in \mathbb{R}^{(s_{eeg}-1) \times N_h} \tag{3.54}$$

and multiplying (3.52) with $\mathbf{T}$ from the left-hand side yields

$$\mathbf{T}\tilde{\mathbf{j}}_h = \mathbf{T}\mathbf{K}_h\tilde{\Phi}_h = \mathbf{R}\mathbf{K}_h^{-1}\mathbf{K}_h\tilde{\Phi}_h = \mathbf{R}\tilde{\Phi}_h = \tilde{\Phi}_{eeg}. \tag{3.55}$$

Thus $\mathbf{T}$ allows a direct mapping of the FE right-hand side to the potential at the electrodes. Remembering that $\tilde{\mathbf{j}}_h$ only has K non-zero entries at the FE nodes neighbouring the source location it can be derived that the calculation of $\mathbf{T}\tilde{\mathbf{j}}_h$ only consists of $2 \cdot (s_{eeg} - 1) \cdot K$ operations.

In order to determine $\mathbf{T}$ the inverse of $\mathbf{K}_h$ must be computed first. This is a difficult task due to the fact that the sparseness of K is lost when inverted. Therefore another approach to computing $\mathbf{T}$ is used. Multiplying (3.54) with $\mathbf{K}_h$ from the right-hand side and transposing both sides yields

$$\mathbf{K}_h\mathbf{T}^T = (\mathbf{T}\mathbf{K}_h)^T = (\mathbf{R}\mathbf{K}_h^{-1}\mathbf{K}_h)^T = \mathbf{R}^T. \tag{3.56}$$

The FE transfer matrix $\mathbf{T}$ can thus be computed by iteratively solving $(s_{eeg} - 1)$ large sparse FE linear equation systems.

With the help of the FE transfer matrix $\mathbf{T}$ as it has been derived in this chapter, the costs for a forward computation at a certain location reduce to a single matrix multiplication with $\mathbf{T}$. The transfer matrix has to be calculated only once and is valid for all possible source locations. As described in [58], a similar concept is possible for the FE based MEG forward problem.

4 Beamformer

Beamformers are a spatial filtering technique that can be applied to solve the EEG/MEG inverse problem. The theory of beamformers will be derived in this chapter.

4.1 Data Model of the Vector Beamformer

This section will describe the idea of vector beamformers and derive some basic formulae as done by Van Veen et al. [49]. It should be mentioned that even though the following description uses the term "electrode" for a sensor (as in EEG), the derived formulae would be the same for the MEG case, where the sensors are magnetometers or gradiometers.

Let $\mathbf{x}$ be an $N \times 1$ vector representing the potentials measured at the N electrode sites at one given instant in time associated with a single dipole source. If this source location is represented by the 3×1 vector $\mathbf{q}$, then $\mathbf{x} = \mathbf{H}(\mathbf{q})\mathbf{m}(\mathbf{q})$ where the elements of the 3×1 vector $\mathbf{m}(\mathbf{q})$ are the x, y and z components of the dipole moment at the instant in time, $\mathbf{x}$ is the theoretical (noisefree) measurement and the columns of the $N \times 3$ leadfield matrix $\mathbf{H}(\mathbf{q})$ represent solutions to the forward problem. More precisely, the first column of $\mathbf{H}(\mathbf{q})$ is the potential at the electrodes due to a dipole source at location $\mathbf{q}$ having unity moment in the x direction and zero moment in y and z direction. Similarly, the second and third columns represent the potential due to sources with unity moment in y and z directions, respectively.

Note that this model for the data applies to electric, magnetic, or combined electric and magnetic measurements. Only the elements of $\mathbf{H}(\mathbf{q})$ depend on the particular sensing modality. In a physical sense, $\mathbf{H}(\mathbf{q})$ represents the material and geometrical properties of the medium in which the sources are submerged.

Because the brain can be considered to be a linear medium, the potential at the scalp is the superposition of the potentials from many active sources. Suppose $\mathbf{x}$ is composed of the potentials due to L active dipole sources at locations $\mathbf{q}_i$, $i = 1, 2, \ldots, L$ and noise. Thus $\mathbf{x}$ can be written as

$$\mathbf{x} = \sum_{i=1}^{L} \mathbf{H}(\mathbf{q}_i)\mathbf{m}(\mathbf{q}_i) + \mathbf{n} \tag{4.1}$$

where $\mathbf{m}(\mathbf{q}_i)$ is the dipole moment at location $\mathbf{q}_i$ and $\mathbf{n}$ is the additive measurement noise. In the limit of $L \to \infty$ the sum may be represented as an integral

over the volume containing possible sources. Note that $\mathbf{x}$ does not contain any temporal information since it is obtained by sampling all electrodes at a single time instant. It represents the spatial distribution of the potential at the measurement sites at the sampling time.

An essential concept of beamformer methods is to treat the $\mathbf{q}_i$ as random variables and describe them in terms of mean and covariance. Different time instances are considered as realizations of these random variables. Specifically, the moment mean vector $\overline{\mathbf{m}}(\mathbf{q}_i)$ and the source covariance matrix $\mathbf{Cov}(\mathbf{q}_i)$ are denoted as

$$\overline{\mathbf{m}}(\mathbf{q}_i) = \mathrm{E}\{\mathbf{m}(\mathbf{q}_i)\} \tag{4.2}$$

$$\mathbf{Cov}(\mathbf{q}_i) = \mathrm{E}\{[\mathbf{m}(\mathbf{q}_i) - \overline{\mathbf{m}}(\mathbf{q}_i)][\mathbf{m}(\mathbf{q}_i) - \overline{\mathbf{m}}(\mathbf{q}_i)]^T\}. \tag{4.3}$$

Assuming that the noise is zero mean ($\mathrm{E}\{\mathbf{n}\} = 0$) with $N \times N$ covariance matrix $\mathbf{Q}$ and that the moments associated with different dipoles are uncorrelated, that is

$$\mathbf{Cov}(\mathbf{q}_i, \mathbf{q}_k) = \mathrm{E}\{[\mathbf{m}(\mathbf{q}_i) - \overline{\mathbf{m}}(\mathbf{q}_i)][\mathbf{m}(\mathbf{q}_k) - \overline{\mathbf{m}}(\mathbf{q}_k)]^T\} = 0 \ \forall i \neq k, \tag{4.4}$$

then the mean of the data vector $\mathbf{x}$ is

$$\begin{aligned}
\overline{\mathbf{x}} &= \mathrm{E}\{\mathbf{x}\} \\
&= \mathrm{E}\left\{\sum_{i=1}^{L} \mathbf{H}(\mathbf{q}_i)\mathbf{m}(\mathbf{q}_i) + \mathbf{n}\right\} \\
&= \sum_{i=1}^{L} \mathrm{E}\{\mathbf{H}(\mathbf{q}_i)\mathbf{m}(\mathbf{q}_i)\} + \mathrm{E}\{\mathbf{n}\} \\
&= \sum_{i=1}^{L} \mathbf{H}(\mathbf{q}_i)\,\mathrm{E}\{\mathbf{m}(\mathbf{q}_i)\} \\
&= \sum_{i=1}^{L} \mathbf{H}(\mathbf{q}_i)\overline{\mathbf{m}}(\mathbf{q}_i)
\end{aligned} \tag{4.5}$$

and the data covariance matrix $\mathbf{C}(\mathbf{x})$ is given by

$$\begin{aligned}
\mathbf{C}(\mathbf{x}) &= \mathrm{E}\{[\mathbf{x} - \overline{\mathbf{x}}][\mathbf{x} - \overline{\mathbf{x}}]^T\} \\
&= \mathrm{E}\left\{ \left[\left(\sum_{i=1}^{L} \mathbf{H}(\mathbf{q}_i)\mathbf{m}(\mathbf{q}_i) + \mathbf{n}\right) - \sum_{i=1}^{L} \mathbf{H}(\mathbf{q}_i)\overline{\mathbf{m}}(\mathbf{q}_i)\right] \right. \\
&\qquad \left. \left[\left(\sum_{i=1}^{L} \mathbf{H}(\mathbf{q}_i)\mathbf{m}(\mathbf{q}_i) + \mathbf{n}\right) - \sum_{i=1}^{L} \mathbf{H}(\mathbf{q}_i)\overline{\mathbf{m}}(\mathbf{q}_i)\right]^T \right\}
\end{aligned}$$

$$
\begin{aligned}
&= \mathrm{E}\left\{ \left[\left(\sum_{i=1}^{L} \mathbf{H}(\mathbf{q}_i)(\mathbf{m}(\mathbf{q}_i) - \overline{\mathbf{m}}(\mathbf{q}_i) \right) + \mathbf{n} \right] \right. \\
&\qquad \left. \left[\left(\sum_{i=1}^{L} \mathbf{H}(\mathbf{q}_i)(\mathbf{m}(\mathbf{q}_i) - \overline{\mathbf{m}}(\mathbf{q}_i) \right) + \mathbf{n} \right]^T \right\} \\
&= \mathrm{E}\left\{ \left[\sum_{i=1}^{L} \mathbf{H}(\mathbf{q}_i)(\mathbf{m}(\mathbf{q}_i) - \overline{\mathbf{m}}(\mathbf{q}_i)) \right] \left[\sum_{i=1}^{L} \mathbf{H}(\mathbf{q}_i)(\mathbf{m}(\mathbf{q}_i) - \overline{\mathbf{m}}(\mathbf{q}_i)) \right]^T \right. \\
&\qquad + \sum_{i=1}^{L} \mathbf{H}(\mathbf{q}_i)(\mathbf{m}(\mathbf{q}_i) - \overline{\mathbf{m}}(\mathbf{q}_i))\mathbf{n}^T \\
&\qquad + \sum_{i=1}^{L} \mathbf{n}(\mathbf{m}(\mathbf{q}_i) - \overline{\mathbf{m}}(\mathbf{q}_i))^T \mathbf{H}^T(\mathbf{q}_i) \\
&\qquad \left. + \mathbf{n}\mathbf{n}^T \right\} \\
&= \mathrm{E}\left\{ \sum_{i=1}^{L} \sum_{j=1}^{L} \mathbf{H}(\mathbf{q}_i)(\mathbf{m}(\mathbf{q}_i) - \overline{\mathbf{m}}(\mathbf{q}_i))(\mathbf{m}(\mathbf{q}_j) - \overline{\mathbf{m}}(\mathbf{q}_j))^T \mathbf{H}^T(\mathbf{q}_j) \right\} + \mathbf{Q} \\
&= \sum_{i=1}^{L} \sum_{j=1}^{L} \mathbf{H}(\mathbf{q}_i) \underbrace{\mathbf{Cov}(\mathbf{q}_i, \mathbf{q}_j)}_{=0 \text{ for } i \neq j} \mathbf{H}^T(\mathbf{q}_j) + \mathbf{Q} \qquad (4.6) \\
&= \sum_{i=1}^{L} \mathbf{H}(\mathbf{q}_i)\mathbf{Cov}(\mathbf{q}_i)\mathbf{H}^T(\mathbf{q}_i) + \mathbf{Q}. \qquad (4.7)
\end{aligned}
$$

The assumption that the moments associated with different dipoles are uncorrelated generally does not hold. The performance of beamformers in the presence of correlated sources will therefore be discussed in Section 4.2.4.

The variance associated with a particular source is defined as a measure of the strength of the source. Here the beamformer differs from other inverse methods for brain source reconstruction that usually measure the source strength by means of source amplitude. Because a scalar value is more convenient to measure source strength, the covariance matrix representing the source variance along the different directions is replaced by its trace

$$tr\{\mathbf{C}(\mathbf{q})\}. \qquad (4.8)$$

In the case of a dipole with fixed orientation this corresponds to the true source variance as show in the following:
The source moment $\mathbf{m}(\mathbf{q})$ can be devided into a dipole orientation $\widetilde{\mathbf{m}}(\mathbf{q})$ and a time dependent source strength $s(t)$

$$\mathbf{m}(\mathbf{q}) = \widetilde{\mathbf{m}}(\mathbf{q})s(t). \qquad (4.9)$$

Then the source covarince is given by ([41])

$$\mathrm{Cov}(\mathbf{q}) = \mathrm{Var}(s)\widetilde{\mathbf{m}}\widetilde{\mathbf{m}}^T \tag{4.10}$$

and $\mathrm{Var}(s)$ is its only nonzero eigenvalue. Because the trace of a matrix is invariant to basis transformation, this yields

$$tr\{\mathrm{Cov}(\mathbf{q})\} = \mathrm{Var}(s). \tag{4.11}$$

As described in Section 3.1, the electric field over the head volume can be expressed by a potential Φ, which is unique up to a constant c. Therefore the EEG measures the potentials at the head surface with respect to a reference electrode. But instead of choosing the reference electrode arbitrarily, it is generally accepted to use common average as defined in the following:
Let $\mathbf{x} = (x_1, ..., x_N)$ be the measurement vector and $\overline{\mathbf{x}} = \frac{1}{N}\sum_{i=1}^{N} x_i$ the mean accross all electrodes. Then the measurement in common average $\tilde{\mathbf{x}}$ is calculated by subtracting $\overline{\mathbf{x}}$ from each sensor measurement, i.e. $\tilde{\mathbf{x}} = (x_1 - \overline{\mathbf{x}}, ..., x_N - \overline{\mathbf{x}})$.

The derivation and discussion that follows is applicable whether or not the data is preprocessed to be in common average notation. For ease of exposition the terms $\mathbf{x}$ and $\mathbf{H}(\mathbf{q})$ will be used.

4.2 Linearly Constrained Minimum Variance Localization

The Linearly Constrained Minimum Variance (LCMV) approach is based on the concept of spatial filtering. Spatial filtering refers to discrimination of signals on the basis of their spatial location. This concept completely parallels the concept of temporal filtering, where one discriminates between signals based on their temporal frequency content. Hence, a "narrow-band" spatial filter passes signals originating from a small "passband" volume while attenuating those originating from other locations. Temporal filtering involves operating on time samples of a signal, whereas spatial filtering involves processing spatial samples of a signal. In the present application, the spatial samples are elements of the data vector $\mathbf{x}$ and the spatial filter is implemented as a weighted combination of these samples. The goal is to design a bank of spatial filters where each filter passes signals originating from a specified location within the brain while attenuating signals from other locations. A display of the variance or power as the output of each filter as a function of the filter's focused location provides an estimate of the distribution of an activity within the brain.

4.2.1 Filter Design

The signal at each location in the brain consists of the three component dipole moment $\mathbf{m}(\mathbf{q}_i)$ which provides information about the strength and the direction

of the dipole. Hence, for each location three spatial filters (one for each component of the dipole moment) will be constructed. The spatial filter focusing on location $\mathbf{q}_0$ is expressed as the $N \times 3$ matrix $\mathbf{W}(\mathbf{q}_0)$. Then the three component filter output $\widehat{\mathbf{m}}$ is given by the inner product of $\mathbf{W}(\mathbf{q}_0)$ and $\mathbf{x}$

$$\widehat{\mathbf{m}} = \mathbf{W}^T(\mathbf{q}_0)\mathbf{x}. \tag{4.12}$$

An ideal narrow-band spatial filter satisfies

$$\mathbf{W}^T(\mathbf{q}_0)\mathbf{H}(\mathbf{q}) = \begin{cases} \mathbf{I}, & \mathbf{q} = \mathbf{q}_0 \\ \mathbf{0}, & \mathbf{q} \neq \mathbf{q}_0 \end{cases}, \mathbf{q} \in \Omega \tag{4.13}$$

where Ω represents the volume of the brain. If (4.13) is satisfied, then in the absence of noise ($\mathbf{n} = \mathbf{0}$) the filter output is $\widehat{\mathbf{m}} = \mathbf{m}(\mathbf{q}_0)$, which is exactly the dipole moment at the location of interest that was to be reconstructed. As in temporal filtering, it is generally impossible to have complete attenuation in the stopband. Unit response in the passband is ensured by requiring

$$\mathbf{W}^T(\mathbf{q}_0)\mathbf{H}(\mathbf{q}_0) = \mathbf{I}. \tag{4.14}$$

Zero response in the stopband implies $\mathbf{W}(\mathbf{q}_0)$ must also satisfy

$$\mathbf{W}^T(\mathbf{q}_0)\mathbf{H}(\mathbf{q}_s) = \mathbf{0} \text{ for } \mathbf{q}_0 \neq \mathbf{q}_s. \tag{4.15}$$

Provided $N \geq 6$ and the columns of $\mathbf{H}(\mathbf{q}_0)$ and $\mathbf{H}(\mathbf{q}_s)$ are linearly independent, it is mathematically possible to simultaneously satisfy (4.14) and (4.15). However, only a limited number of source locations other than $\mathbf{q}_0$ can be completely blocked by the beamformer filter, depending on its degrees of freedom. Each column of $\mathbf{W}(\mathbf{q}_0)$ only has N degrees of freedom. The passband constraint (4.14) uses up three of these, and each independent null uses an additional three so one could at most achieve simultaneous nulls at $N/3-1$ locations having linearly independent leadfield matrices $\mathbf{H}(\mathbf{q})$.

Given the limitations on the stopband attenuation, one naturally asks how to design a filter that is optimal in some sense. The LCMV approach offers a guiding philosophy for designing an optimal filter. The idea is to find a $\mathbf{W}(\mathbf{q}_0)$ that minimizes the variance at the filter output while satisfying the linear response constraint (4.14), hence the name linearly constrained minimum variance.

The constraints ensure that the signals of interest are passed by the filter. Minimization of variance optimally allocates the stopband response of the filter to minimize the contribution to the filter output due to signals in the stopband. This strategy only forces the stopband response to be small at a location $\mathbf{q}_s$ if there is significant energy originating from $\mathbf{q}_s$.

The LCMV problem is posed mathematically as

$$\min_{\mathbf{W}(\mathbf{q}_0)} tr\{\mathbf{C}(\widehat{\mathbf{m}})\} \text{ subject to } \mathbf{W}^T(\mathbf{q}_0)\mathbf{H}(\mathbf{q}_0) = \mathbf{I}. \tag{4.16}$$

Using (4.12) and considering that $\mathbf{W}$ is not a random quantity, $\mathbf{C}(\widehat{\mathbf{m}})$ can be written as (see [41])

$$\mathbf{C}(\widehat{\mathbf{m}}) = \mathbf{C}(\mathbf{W}^T(\mathbf{q}_0)\mathbf{x}) = \mathbf{W}^T(\mathbf{q}_0)\mathbf{C}(\mathbf{x})\mathbf{W}(\mathbf{q}_0). \tag{4.17}$$

Therefore the LCMV problem can also be expressed as

$$\min_{\mathbf{W}(\mathbf{q}_0)} tr\left\{[\mathbf{W}^T(\mathbf{q}_0)\mathbf{C}(\mathbf{x})\mathbf{W}(\mathbf{q}_0)]\right\} \text{ subject to } \mathbf{W}^T(\mathbf{q}_0)\mathbf{H}(\mathbf{q}_0) = \mathbf{I}. \tag{4.18}$$

The solution to (4.18) may be obtained using the methods of Lagrange multipliers. Let $2\mathbf{L}$ be a 3×3 matrix of Lagrange multipliers. The cost function in (4.18) is augmented with the inner product of the Lagrange multipliers and the constraint to obtain the Lagrangian $L(\mathbf{W}, \mathbf{L})$

$$L(\mathbf{W}, \mathbf{L}) = tr\{\mathbf{W}^T\mathbf{C}\mathbf{W} + (\mathbf{W}^T\mathbf{H} - \mathbf{I})2\mathbf{L}\} \tag{4.19}$$

where the arguments $(\mathbf{q}_0)$ and $(\mathbf{x})$ are omitted for clarity. Noting that $tr\{\mathbf{A}\} = tr\{\mathbf{A}^T\}$ for any square matrix $\mathbf{A}$ and that $(\mathbf{BC})^T = \mathbf{C}^T\mathbf{B}^T$ for any two matrices with appropriate dimensions, (4.19) can be rewritten as

$$L(\mathbf{W}, \mathbf{L}) = tr\{\mathbf{W}^T\mathbf{C}\mathbf{W} + (\mathbf{W}^T\mathbf{H} - \mathbf{I})\mathbf{L} + \mathbf{L}^T(\mathbf{H}^T\mathbf{W} - \mathbf{I})\}. \tag{4.20}$$

From this expression we gain

$$\begin{aligned}
L(\mathbf{W}, \mathbf{L}) &= tr\{\mathbf{W}^T\mathbf{C}\mathbf{W} + (\mathbf{W}^T\mathbf{H} - \mathbf{I})\mathbf{L} + \mathbf{L}^T(\mathbf{H}^T\mathbf{W} - \mathbf{I})\} \\
&= tr\{(\mathbf{W}^T\mathbf{C}\mathbf{W} + (\mathbf{W}^T\mathbf{H}\mathbf{L} - \mathbf{L}) + (\mathbf{L}^T\mathbf{H}^T\mathbf{W} - \mathbf{L}^T)\} \\
&= tr\{(\mathbf{W}^T\mathbf{C}\mathbf{W} + \mathbf{W}^T\mathbf{C}\mathbf{C}^{-1}\mathbf{H}\mathbf{L} + \mathbf{L}^T\mathbf{H}^T\mathbf{W} \\
&\quad + \mathbf{L}^T\mathbf{H}^T\mathbf{C}^{-1}\mathbf{H}\mathbf{L} - \mathbf{L} - \mathbf{L}^T - \mathbf{L}^T\mathbf{H}^T\mathbf{C}^{-1}\mathbf{H}\mathbf{L}\} \\
&= tr\{(\mathbf{W}^T\mathbf{C} + \mathbf{L}^T\mathbf{H}^T\mathbf{C}^{-1}\mathbf{C})(\mathbf{W} + \mathbf{C}^{-1}\mathbf{H}\mathbf{L}) - \mathbf{L} - \mathbf{L}^T \\
&\quad - \mathbf{L}^T\mathbf{H}^T\mathbf{C}^{-1}\mathbf{H}\mathbf{L}\} \\
&= tr\{(\mathbf{W}^T + \mathbf{L}^T\mathbf{H}^T\mathbf{C}^{-1})\mathbf{C}(\mathbf{W} + \mathbf{C}^{-1}\mathbf{H}\mathbf{L}) - \mathbf{L} - \mathbf{L}^T \\
&\quad - \mathbf{L}^T\mathbf{H}^T\mathbf{C}^{-1}\mathbf{H}\mathbf{L}\}
\end{aligned} \tag{4.21}$$

by expanding. Here $\mathbf{C}$ was assumed to be invertible (at least in the presence of noise).

Only the first term in the brackets of (4.21) is a function of $\mathbf{W}$. Remembering that $\mathbf{C}$ is a covariance matrix and therefore positive semi-definite, the minimum of $L(\mathbf{W}, \mathbf{L})$ is attained by setting the first term to zero, that is

$$\mathbf{W} = -\mathbf{C}^{-1}\mathbf{H}\mathbf{L}. \tag{4.22}$$

The Lagrange multiplier matrix is now obtained by substituting $\mathbf{W}$ in the constraint $\mathbf{W}^T\mathbf{H} = \mathbf{I}$ to obtain

$$-\mathbf{L}^T\mathbf{H}^T\mathbf{C}^{-1}\mathbf{H} = \mathbf{I} \tag{4.23}$$

or

$$\mathbf{L}^T = -(\mathbf{H}^T\mathbf{C}^{-1}\mathbf{H})^{-1}. \tag{4.24}$$

Note here that $\mathbf{C}$ is a symmetric matrix which yields $\mathbf{C} = \mathbf{C}^T$ and $\mathbf{C}^{-1} = (\mathbf{C}^{-1})^T$. Thereby substituting (4.24) into (4.22) yields the solution

$$\begin{aligned}
\mathbf{W}^T &= [-\mathbf{C}^{-1}\mathbf{H}\mathbf{L}]^T \\
&= [-\mathbf{C}^{-1}\mathbf{H}(-(\mathbf{H}^T\mathbf{C}^{-1}\mathbf{H})^{-1})^T]^T \\
&= [\mathbf{C}^{-1}\mathbf{H}((\mathbf{H}^T\mathbf{C}^{-1}\mathbf{H})^{-1})^T]^T \\
&= (\mathbf{H}^T\mathbf{C}^{-1}\mathbf{H})^{-1}(\mathbf{C}^{-1}\mathbf{H})^T \\
&= (\mathbf{H}^T\mathbf{C}^{-1}\mathbf{H})^{-1}\mathbf{H}^T(C^{-1})^T \\
&= (\mathbf{H}^T\mathbf{C}^{-1}\mathbf{H})^{-1}\mathbf{H}^T\mathbf{C}^{-1},
\end{aligned} \tag{4.25}$$

or more precisely

$$\mathbf{W}^T(\mathbf{q}_0) = [\mathbf{H}^T(\mathbf{q}_0)\mathbf{C}^{-1}(\mathbf{x})\mathbf{H}(\mathbf{q}_0)]^{-1}\mathbf{H}^T(\mathbf{q}_0)\mathbf{C}^{-1}(\mathbf{x}). \tag{4.26}$$

4.2.2 LCMV Localization

Using the filter derived above, namely (4.26), for signal reconstruction as described in (4.12) gives an estimate of the moment at location $\mathbf{q}_0$. The estimated variance or strength of the activity at $\mathbf{q}_0$ is the value of the cost function in (4.16) and (4.18) at the minimum. Omitting $\mathbf{q}_0$ and $\mathbf{x}$ again, the estimation result is therefore given by

$$\begin{aligned}
\widehat{\mathrm{Var}} &= tr\{[\mathbf{W}^T\mathbf{C}\mathbf{W}]\} \\
&= tr\{[\mathbf{H}^T\mathbf{C}^{-1}\mathbf{H}]^{-1}\mathbf{H}^T\mathbf{C}^{-1}\mathbf{C}(\mathbf{C}^{-1})^T\mathbf{H}([\mathbf{H}^T\mathbf{C}^{-1}\mathbf{H}]^{-1})^T\} \\
&= tr\{[\mathbf{H}^T\mathbf{C}^{-1}\mathbf{H}]^{-1}[\mathbf{H}^T(\mathbf{C}^{-1})\mathbf{H}]([\mathbf{H}^T\mathbf{C}^{-1}\mathbf{H}]^{-1})^T\} \\
&= tr\{([\mathbf{H}^T\mathbf{C}^{-1}\mathbf{H}]^{-1})^T\} \\
&= tr\{[\mathbf{H}^T\mathbf{C}^{-1}\mathbf{H}]^{-1}\},
\end{aligned}$$

or in detail

$$\widehat{\mathrm{Var}}(\mathbf{q}_0) = tr\{[\mathbf{H}^T(\mathbf{q}_0)\mathbf{C}^{-1}(\mathbf{x})\mathbf{H}(\mathbf{q}_0)]^{-1}\}. \tag{4.27}$$

To perform localization, the variance or strength is estimated as a function of location within the volume of the brain. This is accomplished by evaluating (4.27) as a function of $\mathbf{q}_0$. Regions of large variance presumably have substantial neural activity. The result in (4.27) is referred to as the estimated "spatial spectrum" of neural activity.

This approach does not require specification or determination of the number of dipole sources to fit to the data. Van Veen et al. [49] suggest that anatomical information can easily be included by only evaluating (4.27) at locations corresponding to physically realistic source locations. As we will show in simulations,

this is rather critical as we are dealing with localizations errors depending on the head model accuracy. This means that the beamformer might find maximum activity at locations that are not physically realistic.

The resolution of detail in the spatial spectrum is ultimately limited by the noise level that has a crucial influence on the minimum "width" or spatial extent of the filter's passband, as we will explain in Section 5.2.2. Two distinct sources that are located within the passband of a particular filter cannot be resolved. The spatial extent of the passband depends on the leadfield matrices $\mathbf{H}(\mathbf{q})$, which in turn depend on the volume conductor, the number of electrodes, their distribution and their source location. Simulations indicate that superficial activity can be resolved with much greater detail than deep activity [49]. The resolution also depends on the SNR associated with the feature of interest. This is a consequence of the variance minimization procedure used to determine the spatial filters. As SNR increases, resolution increases. Note that since the Beamformer is variance based, SNR is defined as the variance of the source divided by the variance of the noise. This is in contrast to the more usual notion of SNR employed in EEG and evoked potential (EP) analysis (see Section 2.4), defined as the ratio of the source signal amplitude to the noise standard deviation.

4.2.3 The Neural Activity Index and Noise

The SNR of measured data is often small, so the sensor noise comprises a significant component of the estimated neural activity obtained using (4.27). Brain noise that appears spatially concentrated or non-uniformly distributed in the spatial spectrum will interfere with localization of actual neural sources. Consider the estimated spatial spectrum assuming $\mathbf{C}(\mathbf{x})$ is due entirely to spatial white (sensor) noise with a mean of $\mu = 0$ and standard deviation $\sigma = 1$, $\mathbf{C}(\mathbf{x}) = \mathbf{I}$. In this case (4.27) simplifies to

$$\widehat{\mathrm{Var}}(\mathbf{q}_0) = tr\{[\mathbf{H}^T(\mathbf{q}_0)\mathbf{H}(\mathbf{q}_0)]^{-1}\}. \tag{4.28}$$

Hence, the noise spatial spectrum depends on the leadfield matrices $\mathbf{H}(\mathbf{q}_0)$. Note that for locations $\mathbf{q}_0$ far from any electrode, the elements of $\mathbf{H}(\mathbf{q}_0)$ are generally quite small, so $[\mathbf{H}^T(\mathbf{q}_0)\mathbf{H}(\mathbf{q}_0)]^{-1}$ will have large elements, resulting in a large value for $\widehat{\mathrm{Var}}(\mathbf{q}_0)$. In contrast, for locations $\mathbf{q}_0$ close to an electrode, $\mathbf{H}(\mathbf{q}_0)$ will have several large elements and $[\mathbf{H}^T(\mathbf{q}_0)\mathbf{H}(\mathbf{q}_0)]^{-1}$ will in general have small elements, resulting in a small value for $\widehat{\mathrm{Var}}(\mathbf{q}_0)$. Because deep source locations are relatively far from electrodes, noise generally has a dome shaped spatial spectrum with the peak of the dome centered at the deepest locations. This dome may be warped significantly if the electrodes are distributed non-uniformly, or if the geometry of the head is assumed to be very non-uniform.

The LCMV spatial spectrum is not linear; that is, the spatial spectrum due to a sum of signals is not the sum of the individual spatial spectra. This is a consequence of the inverses in (4.27). However, application of the matrix

inversion lemma to (4.7) and substitution into (4.27) indicates that (4.27) always contains an additive noise component of the form

$$tr\{[\mathbf{H}^T(\mathbf{q}_0)\mathbf{Q}^{-1}\mathbf{H}(\mathbf{q}_0)]^{-1}\} \tag{4.29}$$

This corresponds to the noise spatial spectrum in the absence of other signals. Due to the relatively low SNRs associated with typical data, the noise spatial spectrum may obscure the spatial spectrum of the neural activity of interest. This problem is reduced by normalizing the estimated spatial spectrum of the data by the estimated noise spatial spectrum to obtain the normalized estimate

$$\widehat{\mathrm{Var}}_N(\mathbf{q}_0) = \frac{tr\{[\mathbf{H}^T(\mathbf{q}_0)\mathbf{C}^{-1}(\mathbf{x})\mathbf{H}(\mathbf{q}_0)]^{-1}\}}{tr\{[\mathbf{H}^T(\mathbf{q}_0)\mathbf{Q}^{-1}\mathbf{H}(\mathbf{q}_0)]^{-1}\}} \tag{4.30}$$

This estimate is termed the *neural activity index*.

The numerator of (4.30) is an estimate of the source plus noise variance at $\mathbf{q}_0$ and the denominator is an estimate of the noise variance at $\mathbf{q}_0$. Hence, the neural activity index may be interpreted as an estimate of the source to noise variance as a function of location. The normalization is a function of location, so the relative levels of estimated neural activity at different locations are changed. In principle, the absolute level can still be determined by reversing the normalization after specific features are identified. The neural activity index requires knowledge of the noise covariance matrix $\mathbf{Q}$. If the noise is assumed to be spatial white noise, i.e. uncorrelated between channels, then $\mathbf{Q} = \sigma^2\mathbf{I}$.

4.2.4 Correlated Sources

Recall that the moments associated with distinct dipoles were assumed to be uncorrelated (4.4). The presence of correlation between distinct sources can lead to reduction of the estimated variance for the sources that are correlated.

Using that (4.6) applies for correlated sources, it can be derived that the output variance at location $\mathbf{q}_k$ is given by

$$\begin{aligned} &tr\{\mathbf{W}^T(\mathbf{q}_k)\mathbf{C}(\mathbf{x})\mathbf{W}(\mathbf{q}_k)\} \\ &\qquad = tr\left\{ \sum_{i=1}^{L}\sum_{n=1}^{L} \mathbf{W}^T(\mathbf{q}_k)\mathbf{H}(\mathbf{q}_i)\mathbf{Cov}(\mathbf{q}_i,\mathbf{q}_n)\mathbf{H}^T(\mathbf{q}_n)\mathbf{W}(\mathbf{q}_k) \right. \\ &\qquad\qquad \left. + \mathbf{W}^T(\mathbf{q}_k)\mathbf{Q}\mathbf{W}(\mathbf{q}_k) \right\} \end{aligned}$$

$$
\begin{aligned}
&= tr\Bigg\{ \sum_{\substack{i=1\\i=k}}^{L}\sum_{\substack{n=1\\n=k}}^{L} \underbrace{\mathbf{W}^T(\mathbf{q}_k)\mathbf{H}(\mathbf{q}_k)}_{=I}\mathbf{Cov}(\mathbf{q}_k,\mathbf{q}_k)\underbrace{\mathbf{H}^T(\mathbf{q}_k)\mathbf{W}(\mathbf{q}_k)}_{=I} \\
&\quad + \sum_{\substack{i=1\\i=k}}^{L}\sum_{\substack{n=1\\n\neq k}}^{L} \underbrace{\mathbf{W}^T(\mathbf{q}_k)\mathbf{H}(\mathbf{q}_k)}_{=I}\mathbf{Cov}(\mathbf{q}_k,\mathbf{q}_n)\mathbf{H}^T(\mathbf{q}_n)\mathbf{W}(\mathbf{q}_k) \\
&\quad + \sum_{\substack{i=1\\i\neq k}}^{L}\sum_{\substack{n=1\\n=k}}^{L} \mathbf{W}^T(\mathbf{q}_k)\mathbf{H}(\mathbf{q}_i)\mathbf{Cov}(\mathbf{q}_i,\mathbf{q}_k)\underbrace{\mathbf{H}^T(\mathbf{q}_k)\mathbf{W}(\mathbf{q}_k)}_{=I} \\
&\quad + \sum_{\substack{i=1\\i\neq k}}^{L}\sum_{\substack{n=1\\n\neq k\\n\neq i}}^{L} \mathbf{W}^T(\mathbf{q}_k)\mathbf{H}(\mathbf{q}_i)\mathbf{Cov}(\mathbf{q}_i,\mathbf{q}_n)\mathbf{H}^T(\mathbf{q}_n)\mathbf{W}(\mathbf{q}_k) \\
&\quad + \mathbf{W}^T(\mathbf{q}_k)\mathbf{Q}\mathbf{W}(\mathbf{q}_k) \Bigg\} \\
&= tr\Bigg\{ \mathbf{C}(\mathbf{q}_k) + \sum_{\substack{i=1\\i\neq k}}^{L} \mathbf{W}^T(\mathbf{q}_k)\mathbf{H}(\mathbf{q}_i)\mathbf{C}(\mathbf{q}_i)\mathbf{H}^T(\mathbf{q}_i)\mathbf{W}(\mathbf{q}_k) \\
&\quad + \sum_{\substack{i=1\\i\neq k}}^{L}[\mathbf{C}(\mathbf{q}_k,\mathbf{q}_i)\mathbf{H}^T(\mathbf{q}_i)\mathbf{W}(\mathbf{q}_k) \\
&\qquad\qquad + \mathbf{W}^T(\mathbf{q}_k)\mathbf{H}(\mathbf{q}_i)\mathbf{C}(\mathbf{q}_i,\mathbf{q}_k)] \\
&\quad + \sum_{\substack{n,i=1\\n,i\neq k\\n\neq i}}^{L} [\mathbf{W}^T(\mathbf{q}_k)[\mathbf{H}(\mathbf{q}_i)\mathbf{C}(\mathbf{q}_i,\mathbf{q}_n)\mathbf{H}^T(\mathbf{q}_n) \\
&\qquad\qquad + \mathbf{H}(\mathbf{q}_n)\mathbf{C}(\mathbf{q}_n,\mathbf{q}_i)\mathbf{H}^T(\mathbf{q}_i)]\mathbf{W}(\mathbf{q}_k)] \\
&\quad + \mathbf{W}^T(\mathbf{q}_k)\mathbf{Q}\mathbf{W}(\mathbf{q}_k) \Bigg\}. \qquad (4.31)
\end{aligned}
$$

The cross terms on the right-hand side of (4.31) are not guaranteed to be positive for all $\mathbf{W}(\mathbf{q}_k)$. Recall that the LCMV criterion chooses a $\mathbf{W}(\mathbf{q}_k)$ to minimize (4.31). The minimum is in general obtained with a $\mathbf{W}(\mathbf{q}_k)$ that would turn the cross terms to be negative. If this occurs, then the estimated variance of the source at $\mathbf{q}_k$, $tr\{\mathbf{W}^T(\mathbf{q}_k)\mathbf{C}(\mathbf{x})\mathbf{W}(\mathbf{q}_k)\}$, is significantly smaller than its true value $tr\{\mathbf{C}(\mathbf{q}_k)\}$. For full correlation it turns out that $tr\{\mathbf{W}^T(\mathbf{q}_k)\mathbf{C}(\mathbf{x})\mathbf{W}(\mathbf{q}_k)\} = 0$ holds. The spatial filter exploits the correlation between sources to minimize

output variance by canceling the correlated portion of the source of interest. Correlated source cancellation is a phenomenon that is well known in adaptive beamforming applications of the LCMV method for radar and sonar [52]. Perfect correlation between spatially distinct sources in the brain is unlikely, although partial correlation is expected in certain situations, such as when several brain areas react to an external stimulus or become activated by a common third active area.

The performance of beamformers in the presence of correlated source activity has been investigated by Sekihara et al. in [43]. They have shown that the reductions in the reconstructed signal intensities is small for sources with a medium degree of correlation (less than 20% for two correlated sources with a correlation coefficient of less than 0.6). Even for significantly correlated sources (correlation coefficients of $0.7 - 0.8$) can still be reconstructed if their intensities are strong enough to overcome the signal cancellation [43].

4.3 Synthetic Aperture Magnetometry (SAM)

As described above, the LCMV Beamformer approach does not make any prior assumption on the direction of the dipole moment for a given source location $\mathbf{q}$. The SAM approach significantly differs from LCMV in the sense that SAM tries to estimate the dipole direction at source location $\mathbf{q}$ in advance, hence that the Beamformer weights are only computed for one distinct direction. In this case the spatial filter $\mathbf{W}(\mathbf{q})$ is no longer a $N \times 3$ matrix but a $N \times 1$ weight vector. The determination of the dipole direction will be described in this section.

The idea of SAM is to find a dipole orientation at which some beamformer parameter is optimal (see [50]). In this derivation the parameter to be optimized is the pseudo-Z value that will be introduced in this section. In order to find the dipole orientation that maximizes the pseudo-Z value for a given source location the formulae derived above are going to be considered for a fixed dipole orientation. The notations used above will be maintained throughout this chapter.

Assuming that the dipole orientation at location $\mathbf{q}$ is given by a 3×1 vector $\mathbf{e}$, the dipole moment at $\mathbf{q}$ can be written as $\mathbf{m}(\mathbf{q}) = a\mathbf{e}$ for a scalar value a. The $N \times 3$ transfer matrix $\mathbf{H}(\mathbf{q})$ reduces to a $N \times 1$ transfer vector

$$\mathbf{h} = \mathbf{H}(\mathbf{q})\mathbf{e} \tag{4.32}$$

and the spatial filter in equation (4.26) simplifies to

$$\mathbf{w}^T = \frac{\mathbf{h}^T\mathbf{C}^{-1}}{\mathbf{h}^T\mathbf{C}^{-1}\mathbf{h}}. \tag{4.33}$$

As in the LCMV approach we have to account for projected sensor noise again. Instead of the neural activity index introduced by van Veen et al. [49], SAM typically uses so-called pseudo-Z values which represent the estimated spatial

spectrum of the data normalized by the beamformer projected noise. Like in (4.27) the estimated spatial spectrum of the data can be written as

$$\widehat{\mathrm{Var}}(\mathbf{q}) = \frac{1}{\mathbf{h}^T\mathbf{C}^{-1}\mathbf{h}}. \tag{4.34}$$

Note that unlike in (4.27) the trace does not need to be considered, as the argument obtained is now a scalar value and not a matrix. The noise spatial spectrum is derived as follows.

Assuming that the noise is distributed with zero mean and variance σ^2 and uncorrelated for all sensors, the noise covariance matrix $\mathbf{Q}$ can be written as

$$\mathbf{Q} = \sigma^2\mathbf{I}, \tag{4.35}$$

where $\mathbf{I}$ corresponds to the N-dimensional identity matrix. In practice σ^2 is often chosen to be the smallest eigenvalue of the data covariance matrix $\mathbf{C}$. The noise spatial spectrum is now obtained by applying the spatial filter $\mathbf{w}$ to the noise covariance matrix (4.35)

$$\eta^2 = \mathbf{w}^T\sigma^2\mathbf{I}\mathbf{w} = \sigma^2\mathbf{w}^T\mathbf{w}. \tag{4.36}$$

In order to write (4.36) in full detail, note that

$$\begin{aligned}
\mathbf{w} = (\mathbf{w}^T)^T &= (\mathbf{h}^T\mathbf{C}^{-1}(\mathbf{h}^T\mathbf{C}^{-1}\mathbf{h})^{-1})^T \\
&= \underbrace{((\mathbf{h}^T\mathbf{C}^{-1}\mathbf{h})^{-1})^T}_{((\mathbf{h}^T\mathbf{C}^{-1}\mathbf{h})^T)^{-1}}(\mathbf{h}^T\mathbf{C}^{-1})^T \\
&= \frac{\mathbf{C}^{-1}\mathbf{h}}{(\mathbf{h}^T\mathbf{C}^{-1}\mathbf{h})^T} \\
&= \frac{\mathbf{C}^{-1}\mathbf{h}}{(\mathbf{h}^T\mathbf{C}^{-1}\mathbf{h})}
\end{aligned} \tag{4.37}$$

and therefore

$$\eta^2 = \sigma^2\frac{\mathbf{h}^T\mathbf{C}^{-1}}{\mathbf{h}^T\mathbf{C}^{-1}\mathbf{h}}\frac{\mathbf{C}^{-1}\mathbf{h}}{(\mathbf{h}^T\mathbf{C}^{-1}\mathbf{h})} = \sigma^2\frac{\mathbf{h}^T\mathbf{C}^{-2}\mathbf{h}}{(\mathbf{h}^T\mathbf{C}^{-1}\mathbf{h})^2}. \tag{4.38}$$

Using (4.34) and (4.38) the pseudo-Z notation is given as

$$\widehat{\mathrm{Var}_N} = \frac{1}{\mathbf{h}^T\mathbf{C}^{-1}\mathbf{h}}\frac{(\mathbf{h}^T\mathbf{C}^{-1}\mathbf{h})^2}{\sigma^2\mathbf{h}^T\mathbf{C}^{-2}\mathbf{h}} = \frac{\mathbf{h}^T\mathbf{C}^{-1}\mathbf{h}}{\sigma^2\mathbf{h}^T\mathbf{C}^{-2}\mathbf{h}} \tag{4.39}$$

The next crucial step to actually finding the optimal dipole direction is to interpret (4.39) as a function of dipole orientation. For this purpose equality (4.32) is used which results in

$$\widehat{\mathrm{Var}_N}(\mathbf{e}) = \frac{\mathbf{e}^T\mathbf{H}^T\mathbf{C}^{-1}\mathbf{H}\mathbf{e}}{\sigma^2\mathbf{e}^T\mathbf{H}^T\mathbf{C}^{-2}\mathbf{H}\mathbf{e}} \tag{4.40}$$

$$= \frac{\mathbf{e}^T\mathbf{A}\mathbf{e}}{\sigma^2\mathbf{e}^T\mathbf{B}\mathbf{e}}, \tag{4.41}$$

with $\mathbf{A} = \mathbf{H}^T\mathbf{C}^{-1}\mathbf{H}$ and $\mathbf{B} = \mathbf{H}^T\mathbf{C}^{-2}\mathbf{H}$. It becomes obvious that (4.40) is the generalized Rayleigh Quotient. Hence, the dipole direction maximizing the neural activity index is given by an eigenvector $\mathbf{e}_0$ corresponding to the biggest eigenvalue of $\mathbf{B}^{-1}\mathbf{A}$ and

$$\widehat{\mathrm{Var}_N}(\mathbf{e}_0) = \max_{\mathbf{e}} \widehat{\mathrm{Var}_N}(\mathbf{e}). \tag{4.42}$$

4.4 Covariance Matrix Error and Finite Integration

From (4.26) and (4.33) it becomes obvious that the beamformer spatial filters – and therefore also the source reconstruction – directly depend on the data covariance matrix. The data covariance matrix that is used to compute the filter weights is a data driven estimation of the true data covariance matrix.

As described by Brookes et al. in [6] the accuracy of the covariance matrix is crucial and e.g. for MEG it particularly depends on crosstalk between neighbouring sensors, errors in the gain of the system amplifiers, inaccurate synchronisation of channels and so on. A crucial parameter that affects the covariance accuracy is the amount of data used to create the covariance estimate, which will also be denoted as the integration window or covariance window. Ideally, covariance would be computed as the infinite integration limit in order to give a perfect representation of signal power. In practice though, for localisation of spontaneous, evoked or induced brain activity, integration windows can only be a few hundred milliseconds long per trial. This is affecting the accuracy of covariance estimation and therefore the accuracy of the source power estimates and reconstructed volumetric images.

In the following the results of [6] will be discussed. Although [6] focuses on MEG, the main principles should also apply for the EEG that we are concentrating on.

As mentioned before, the beamformer weights and thereby the beamformer estimate of source amplitude are dependent on the data covariance matrix $\mathbf{C}$ and the forward solution given by the leadfield matrix $\mathbf{H}$. Assuming an accurate forward solution, the accuracy of the beamformer entirely depends on the data covariance matrix. Consider now the case in which a single source is active with forward solution $\mathbf{h}$ and variance ρ^2. Using (4.7) an analytical form for the covariance matrix in the infinite integration limit is given by

$$\mathbf{C}_0 = \rho^2\mathbf{h}\mathbf{h}^T + \sigma^2\mathbf{I}. \tag{4.43}$$

Again $\mathbf{Q} = \sigma^2\mathbf{I}$ represents the covariance matrix of the sensor noise in the case of spatial white noise with power σ^2 at all MEG channels. The first term in (4.43)

represents the genuine source power, whereas the second term is representative of the uncorrelated noise power.

In practice the data covariance matrix is unknown since the source location and orientation are unknown. Therefore it must be estimated from the data. A commonly used estimate of the covariance measured between two channels i and j is

$$\mathbf{C}_{ij} = \frac{1}{K}\sum_{l=1}^{K}(m_i(t_l))(m_j(t_l)), \tag{4.44}$$

where K is the number of samples recorded during the time window t_{cov}, $m_i(t_l)$ represents the lth magnetic field measurement from channel i and $m_j(t_l)$ represents the lth magnetic field measurement for channel j respectively. It is assumed here that the magnetic field measurements have zero mean. A useful rule of thumb is that the number of samples (K) must be greater than the total number of channels in the system (N) in order for $\mathbf{C}$ to remain non-singular, and therefore invertible for (4.26). Furthermore, it is suggested in [49] that if $\mathbf{C}$ is constructed from a random process, increasing the number of recorded samples K decreases the amount of randomness (hence, inaccuracies in the estimation of covariance). In the following the aim is to relate these inaccuracies quantitatively to the integration window.

First Brookes et al. [6] introduce the concept of covariance matrix error $\Delta\mathbf{C}$. It is defined such that

$$\Delta\mathbf{C} = \mathbf{C} - \mathbf{C}_0, \tag{4.45}$$

where $\mathbf{C}$ represents the data-derived covariance matrix from (4.44) and $\mathbf{C}_0$ the analytically derived covariance matrix given by (4.43). Note here that, written in this form, covariance matrix errors may not be solely due to finite integration time, but may also contain components due to gain error, inaccurate synchronization of channels or crosstalk. In the following however, only the effect of finite integration time will be taken into account.

Generally $m_i(t_l)$ is given by [6]

$$m_i(t_l) = m_{0i}(t_l) + \eta_i(t_l), \tag{4.46}$$

where m_{0i} represents a noiseless measurement of the magnetic field at the ith channel and η_i represents the effect of sensor noise at the ith channel and therefore the error in the measurement. In the following the sensor noise is assumed to have zero mean, i.e. $\overline{\eta}_i = 0$. The elements of the data covariance matrix are given by substituting (4.46) into (4.44), thus

$$\mathbf{C}_{ij} = \frac{1}{K}\sum_{l=1}^{K}[m_{0i}(t_l) + \eta_i(t_l)][m_{0j}(t_l) + \eta_j(t_l)] \tag{4.47}$$

holds. Expanding product and sum yields

$$\mathbf{C}_{ij} = \mathbf{C}_{0ij} + \Delta\mathbf{C}_{ij}, \tag{4.48}$$

where $\mathbf{C}_{0ij} = \frac{1}{K}\sum_{l=1}^{K} m_{0i}(t_l)m_{0j}(t_l)$ (Brookes et al. [6] assume that due to the sampling theorem the estimator on the right-hand side is equal to the analytical C_{0ij} from equation (4.45) for K sufficiently large) and $\Delta\mathbf{C}_{ij} = A_1 + A_2 + A_3$ with

$$A_1 = \frac{1}{K}\sum_{l=1}^{K} m_{0i}(t_l)\eta_j(t_l)$$

$$A_2 = \frac{1}{K}\sum_{l=1}^{K} m_{0j}(t_l)\eta_i(t_l)$$

$$A_3 = \frac{1}{K}\sum_{l=1}^{K} \eta_i(t_l)\eta_j(t_l).$$

It follows that $\Delta\mathbf{C}_{ij}$ represents the elements of the covariance matrix error and in the limit of infinite integration $\Delta\mathbf{C}_{ij}$ will tend to zero due to the facts that sensor noise is uncorrelated for different channels and that the noise and the signal are uncorrelated. For finite integration times $\Delta\mathbf{C}_{ij}$ will be finite and under the assumption in [6] that the processes A_1, A_2 and A_3 are uncorrelated, the magnitude of these covariance error elements $\Delta\mathbf{C}_{ij}$ can be represented by samples from a random process with variance given by

$$\mathrm{Var}(\Delta\mathbf{C}_{ij}) = \mathrm{Var}(A_1) + \mathrm{Var}(A_2) + \mathrm{Var}(A_3). \tag{4.49}$$

The assumption that the processes A_1, A_2 and A_3 are uncorrelated is generally not fulfilled. For $i = j$ we obviously have $A_1 = A_2$, which is highly correlated. Therefore we will take a closer look at the cases $i \neq j$ and $i = j$. The properties derived in the following can easily be shown under the assumption that the noise η_i at channel i is stochastically independent (st. i.) to processes depending on noise from other channels and/or any brain source signal, including the signal m_{0i} at the ith sensor. We further assumed that processes depending on the noise at different instances in time are stochastically independent, i.e. processes depending on $\eta_i(t_l)$ and $\eta_i(t_r)$ are stochastically independent for $l \neq r$. The noise is assumed to have zero mean.

Let $i \neq j$. In this case A_1 is uncorrelated to A_2 and A_3:

$$\begin{aligned}
\mathrm{Cov}(A_1, A_2) &= \mathrm{E}[A_1A_2] - \mathrm{E}[A_1]\,\mathrm{E}[A_2] \\
&= \mathrm{E}[A_1A_2] - \mathrm{E}\left[\frac{1}{K}\sum_{l=1}^{K} m_{0j}(t_l)\eta_i(t_l)\right]\mathrm{E}[A_2] \\
&= \mathrm{E}[A_1A_2] - \left[\frac{1}{K}\sum_{l=1}^{K} \underbrace{\mathrm{E}[m_{0j}(t_l)\eta_i(t_l)]}_{\underbrace{\mathrm{E}[m_{0j}(t_l)]}_{0}\,\mathrm{E}[\eta_i(t_l)]\ \text{(st. i.)}}\right]\mathrm{E}[A_2]
\end{aligned}$$

$$
\begin{aligned}
&= \mathrm{E}[A_1 A_2] - 0 \\
&= \mathrm{E}\left[\frac{1}{K^2}\sum_{r=1}^{K}\sum_{l=1}^{K} m_{0j}(t_l)\eta_i(t_l)m_{0i}(t_r)\eta_j(t_r)\right] \\
&= \frac{1}{K^2}\sum_{r=1}^{K}\sum_{l=1}^{K} \mathrm{E}[m_{0j}(t_l)\eta_i(t_l)m_{0i}(t_r)\eta_j(t_r)] \text{ (st. i.)} \\
&= \frac{1}{K^2}\sum_{r=1}^{K}\sum_{l=1}^{K} \mathrm{E}[m_{0j}(t_l)\eta_i(t_l)m_{0i}(t_r)]\,\underbrace{\mathrm{E}[\eta_j(t_r)]}_{0} \\
&= 0
\end{aligned} \tag{4.50}
$$

and

$$
\begin{aligned}
\mathrm{Cov}(A_1, A_3) &= \mathrm{E}[A_1 A_3] - \mathrm{E}[A_1]\,\mathrm{E}[A_3] \\
&= \mathrm{E}[A_1 A_3] - 0\,\mathrm{E}[A_3] \\
&= \mathrm{E}\left[\frac{1}{K^2}\sum_{r=1}^{K}\sum_{l=1}^{K} m_{0i}(t_l)\eta_j(t_l)\eta_i(t_r)\eta_j(t_r)\right] \\
&= \frac{1}{K^2}\sum_{r=1}^{K}\sum_{l=1}^{K} \mathrm{E}[m_{0i}(t_l)\eta_j(t_l)\eta_i(t_r)\eta_j(t_r)] \text{ (st. i.)} \\
&= \frac{1}{K^2}\sum_{r=1}^{K}\sum_{l=1}^{K} \underbrace{\mathrm{E}[m_{0i}(t_l)]}_{0}\,\mathrm{E}[\eta_j(t_l)\eta_i(t_r)\eta_j(t_r)] \\
&= 0.
\end{aligned} \tag{4.51}
$$

A_2 and A_3 are shown to be uncorrelated analogously, so that (4.49) holds for $i \neq j$.

Let $i = j$. Then $A_1 = A_2$ and A_1 is uncorrelated with A_3:

$$
\begin{aligned}
\mathrm{Cov}(A_1, A_3) &= \mathrm{E}[A_1 A_3] - \mathrm{E}[A_1]\,\mathrm{E}[A_3] \\
&= \mathrm{E}[A_1 A_3] - 0\,\mathrm{E}[A_3] \\
&= \mathrm{E}\left[\frac{1}{K^2}\sum_{r=1}^{K}\sum_{l=1}^{K} m_{0i}(t_l)\eta_i(t_l)\eta_i^2(t_r)\right] \\
&= \frac{1}{K^2}\sum_{r=1}^{K}\sum_{l=1}^{K} \mathrm{E}[m_{0i}(t_l)\eta_i(t_l)\eta_i^2(t_r)] \text{ (st. i.)} \\
&= \frac{1}{K^2}\sum_{r=1}^{K}\sum_{l=1}^{K} \underbrace{\mathrm{E}[m_{0i}(t_l)]}_{0}\,\mathrm{E}[\eta_i(t_l)\eta_i^2(t_r)] \\
&= 0.
\end{aligned} \tag{4.52}
$$

In this case $\Delta\mathbf{C}_{ii} = 2A_1 + A_3$ holds and (4.49) must be rewritten to

$$\begin{aligned}\operatorname{Var}(\Delta\mathbf{C}_{ij}) &= \operatorname{Var}(2A_1 + A_3)\\ &= \operatorname{Var}(2A_1) + \operatorname{Var}(A_3)\\ &= 4\operatorname{Var}(A_1) + \operatorname{Var}(A_3)\\ &= 2(\operatorname{Var}(A_1) + \operatorname{Var}(A_2)) + \operatorname{Var}(A_3)\end{aligned} \tag{4.53}$$

for $i = j$. Note here that $\operatorname{Var}(aX) = a^2 \operatorname{Var}(X)$ for a random quantity X and a scalar value a.

The following analysis can now be developed by recognizing that the summations in (**??**) are related to correlation coefficients. As proposed in [6] and derived in the following, the term A_3 for example can be rewritten as

$$A_3 = \frac{1}{K}\sum_{l=1}^{K} \eta_i(t_l)\eta_j(t_l) = \frac{\widehat{r}(\eta_i, \eta_j)\|\eta_i\|_F\|\eta_j\|_F}{K}, \tag{4.54}$$

where $\widehat{r}(\eta_i, \eta_j)$ is the empirical correlation coefficient between η_i and η_j, and $\|\eta_i\|_F$ and $\|\eta_j\|_F$ are the Frobenius norms of η_i and η_j respectively. With $\operatorname{Std}(X)$ representing the standard deviation of argument X, the equality in (4.54) can be shown by replacing $\widehat{r}(\eta_i, \eta_j)$, $\|\eta_i\|_F$ and $\|\eta_j\|_F$ by their definitions and assuming that the noise has zero mean:

$$\begin{aligned}\frac{\widehat{r}(\eta_i, \eta_j)\|\eta_i\|_F\|\eta_j\|_F}{K} &= \frac{\widehat{\operatorname{Cov}}(\eta_i, \eta_j)}{\widehat{\operatorname{Std}}(\eta_i)\widehat{\operatorname{Std}}(\eta_j)} \cdot \frac{\|\eta_i\|_F\|\eta_j\|_F}{K}\\ &= \widehat{\operatorname{Cov}}(\eta_i, \eta_j) \cdot \frac{\|\eta_i\|_F\|\eta_j\|_F}{K\widehat{\operatorname{Std}}(\eta_i)\widehat{\operatorname{Std}}(\eta_j)}\\ &= \widehat{\operatorname{Cov}}(\eta_i, \eta_j) \cdot \frac{\sqrt{\sum_{l=1}^{K}\eta_i^2(t_l)}\sqrt{\sum_{l=1}^{K}\eta_j^2(t_l)}}{K \cdot \frac{1}{K}\sqrt{\sum_{l=1}^{K}\eta_i^2(t_l)}\sqrt{\sum_{l=1}^{K}\eta_j^2(t_l)}}\\ &= \widehat{\operatorname{Cov}}(\eta_i, \eta_j) \cdot 1\\ &= \frac{1}{K}\sum_{l=1}^{K}\eta_i(t_l)\eta_j(t_l).\end{aligned} \tag{4.55}$$

The symbol $\widehat{\cdot}$ again indicates empirical quantities.

The Frobenius norms $\|\eta_i\|_F$ and $\|\eta_j\|_F$ are related to the root mean square (RMS) value of the uncorrelated noise at each MEG sensor such that, if σ_i represents the level of the uncorrelated noise at sensor i, then

$$\|\eta_i\|_F = \sqrt{\sum_{l=1}^{K}\eta_i^2(t_l)} \approx \sqrt{\sigma_i^2 K} = \sigma_i\sqrt{K}. \tag{4.56}$$

Since η_i and η_j are uncorrelated random processes, $r(\eta_i, \eta_j) \to 0$ holds in the limit of infinite integration. For finite integration times however, Brookes et al. [6] argue that the standard deviation of the correlation coefficient $\mathrm{Std}(\widehat{r}(\eta_i, \eta_j))$ is given by (see [3])

$$\mathrm{Std}(\widehat{r}(\eta_i, \eta_j)) = \frac{1}{\sqrt{K}} \text{ for } i \neq j \tag{4.57}$$

and

$$\mathrm{Std}(\widehat{r}(\eta_i, \eta_j)) = \frac{2}{\sqrt{K}} \text{ for } i = j. \tag{4.58}$$

Note that the correlation coefficient in (4.57) is defined as $\frac{\widehat{\mathrm{Cov}}(\eta_i,\eta_j)}{\mathrm{Std}(\eta_i)\,\mathrm{Std}(\eta_j)}$ and not as $\frac{\widehat{\mathrm{Cov}}(\eta_i,\eta_j)}{\widehat{\mathrm{Std}}(\eta_i)\widehat{\mathrm{Std}}(\eta_j)}$ as in (4.55). The autocorrelation coefficient in (4.58) is defined analogously. Combining (4.54)-(4.58) gives

$$\mathrm{Std}(A_3) \approx \frac{\sigma_i \sigma_j}{\sqrt{K}} \text{ for } i \neq j \tag{4.59}$$

and

$$\mathrm{Std}(A_3) \approx \sqrt{\frac{2}{K}} \sigma_i^2 \text{ for } i = j. \tag{4.60}$$

This is validated by

$$\begin{aligned}
\mathrm{Std}(A_3) &= \sqrt{\mathrm{Var}(A_3)} \\
&= \sqrt{\mathrm{Var}\left(\frac{\widehat{r}(\eta_i, \eta_j)\|\eta_i\|_F \|\eta_j\|_F}{K}\right)} \\
&\approx \sqrt{\mathrm{Var}\left(\frac{\widehat{r}(\eta_i, \eta_j)\sigma_i\sqrt{K}\sigma_j\sqrt{K}}{K}\right)} \\
&= \sqrt{\frac{\sigma_i^2\sigma_j^2K^2}{K^2}\,\mathrm{Var}(\widehat{r}(\eta_i, \eta_j))} \\
&= \sigma_i\sigma_j\sqrt{\mathrm{Var}(\widehat{r}(\eta_i, \eta_j))} \\
&= \sigma_i\sigma_j\,\mathrm{Std}(\widehat{r}(\eta_i, \eta_j)) \\
&= \begin{cases} \frac{\sigma_i\sigma_j}{\sqrt{K}} & i \neq j \\ \sqrt{\frac{2}{K}}\sigma_i^2, & i = j. \end{cases}
\end{aligned} \tag{4.61}$$

The standard deviations of A_1 and A_2 are derived in a similar way. A_1 can be

rewritten to

$$\begin{aligned} A_1 &= \frac{1}{K}\sum_{l=1}^{K} m_{0i}(t_l)\eta_j(t_l) \\ &= \widehat{\mathrm{Cov}}(m_{0i},\eta_j) \\ &= \widehat{r}(m_{0i},\eta_j)\widehat{\mathrm{Std}}(m_{0i})\widehat{\mathrm{Std}}(\eta_j) \\ &= \widehat{r}(m_{0i},\eta_j)\widehat{\mathrm{Std}}(m_{0i})\frac{\|\eta_j\|_F}{\sqrt{K}}. \end{aligned} \tag{4.62}$$

Here $\widehat{\mathrm{Std}}(m_{0i})$ represents the standard deviation of the noiseless field measurements at sensor i and is given by

$$\widehat{\mathrm{Std}}(m_{0i}) = \sqrt{\frac{1}{K}\sum_{i=1}^{K}(m_{0i}(t_l))^2} \approx \rho^2 \mathbf{h}_i, \tag{4.63}$$

with $\mathbf{h}_i$ representing the forward solution to the fixed dipole at the ith sensor. Analogous to equation (4.57), we have

$$\mathrm{Std}(\widehat{r}(m_{0i},\eta_j)) = \frac{1}{\sqrt{K}}. \tag{4.64}$$

Together with (4.56) and (4.62) this concludes to

$$\begin{aligned} \mathrm{Std}(A_1) &= \sqrt{\mathrm{Var}(A_1)} \\ &= \sqrt{\mathrm{Var}\left(\widehat{r}(m_{0i},\eta_j)\widehat{\mathrm{Std}}(m_{0i})\frac{\|\eta_j\|}{\sqrt{K}}\right)} \\ &\approx \sqrt{\mathrm{Var}\left(\widehat{r}(m_{0i},\eta_j)\widehat{\mathrm{Std}}(m_{0i})\frac{\sigma_j\sqrt{K}}{\sqrt{K}}\right)} \\ &= \sqrt{\widehat{\sigma}^2(m_{0i})\sigma_j^2\,\mathrm{Var}(\widehat{r}(m_{0i},\eta_j))} \\ &= \widehat{\mathrm{Std}}(m_{0i})\sigma_j\sqrt{\mathrm{Var}(\widehat{r}(m_{0i},\eta_j))} \\ &= \widehat{\mathrm{Std}}(m_{0i})\sigma_j\frac{1}{\sqrt{K}} \\ &= \frac{\widehat{\mathrm{Std}}(m_{0i})\sigma_j}{\sqrt{K}}. \end{aligned} \tag{4.65}$$

The standard deviation of A_2

$$\mathrm{Std}(A_2) \approx \frac{\widehat{\mathrm{Std}}(m_{0j})\sigma_i}{\sqrt{K}} \tag{4.66}$$

is derived analogously.

Considering the case in which the noise level is equal at all channels (i.e. $\sigma_i = \sigma_j = \sigma$), substitution of (4.61), (4.65) and (4.66) into (4.49) yields

$$\begin{aligned}
\mathrm{Var}(\Delta\mathbf{C}_{ij}) &= \mathrm{Var}(A_1) + \mathrm{Var}(A_2) + \mathrm{Var}(A_3) \\
&= [\mathrm{Std}(A_1)]^2 + [\mathrm{Std}(A_2)]^2 + [\mathrm{Std}(A_3)]^2 \\
&\approx \left[\frac{\widehat{\mathrm{Std}}(m_{0i})\sigma}{\sqrt{K}}\right]^2 + \left[\frac{\widehat{\mathrm{Std}}(m_{0j})\sigma}{\sqrt{K}}\right]^2 + \left[\sqrt{\frac{1}{K}}\sigma^2\right]^2 \\
&= \frac{\sigma^2}{K}\left\{[\widehat{\mathrm{Std}}(m_{0i})]^2 + [\widehat{\mathrm{Std}}(m_{0j})]^2 + \sigma^2\right\}
\end{aligned} \tag{4.67}$$

is obtained for $i \neq j$.

By substituting (4.61), (4.65) and (4.66) into (4.53), we obtain

$$\begin{aligned}
\mathrm{Var}(\Delta\mathbf{C}_{ij}) &= 2\,\mathrm{Var}(A_1) + 2\,\mathrm{Var}(A_2) + \mathrm{Var}(A_3) \\
&= 2[\mathrm{Std}(A_1)]^2 + 2[\mathrm{Std}(A_2)]^2 + [\mathrm{Std}(A_3)]^2 \\
&\approx 2\left[\frac{\widehat{\mathrm{Std}}(m_{0i})\sigma}{\sqrt{K}}\right]^2 + 2\left[\frac{\widehat{\mathrm{Std}}(m_{0j})\sigma}{\sqrt{K}}\right]^2 + \left[\sqrt{\frac{2}{K}}\sigma^2\right]^2 \\
&= \frac{\sigma^2}{K}\left\{2[\widehat{\mathrm{Std}}(m_{0i})]^2 + 2[\widehat{\mathrm{Std}}(m_{0j})]^2 + 2\sigma^2\right\} \\
&= \frac{2\sigma^2}{K}\left\{[\widehat{\mathrm{Std}}(m_{0i})]^2 + [\widehat{\mathrm{Std}}(m_{0j})]^2 + \sigma^2\right\}
\end{aligned} \tag{4.68}$$

for $i = j$. Note that $\mathrm{Var}(\Delta\mathbf{C}_{ij})$ for $i = j$ and for $i \neq j$ only differ by a factor of two.

The equation above represents the standard deviation of the elements of the covariance matrix error $\Delta\mathbf{C}_{ij}$. It is now desirable to derive a scalar parameter that is representative of the error in the covariance estimate across the entirety of $\Delta\mathbf{C}$.

Using $\mathrm{E}[\Delta\mathbf{C}_{ij}] = 0$, the expected Frobenius norm of the covariance matrix error is given by

$$\begin{aligned}
\mathrm{E}[\|\Delta\mathbf{C}\|_F] &= \mathrm{E}[\sqrt{\sum_{i=1}^{N}\sum_{j=1}^{N}\Delta\mathbf{C}_{ij}^2}] \\
&= \sqrt{\sum_{i=1}^{N}\sum_{j=1}^{N}\mathrm{E}[\Delta\mathbf{C}_{ij}^2]} \\
&= \sqrt{\sum_{i=1}^{N}\sum_{j=1}^{N}\mathrm{Var}(\Delta\mathbf{C}_{ij})}
\end{aligned}$$

$$= \sqrt{\sum_{i=1}^{N}\sum_{\substack{j=1\\ j\neq i}}^{N} \mathrm{Var}(\Delta\mathbf{C}_{ij}) + \sum_{i=1}^{N} \mathrm{Var}(\Delta\mathbf{C}_{ii})}$$

$$\approx \frac{\sigma}{\sqrt{K}} \left(\sum_{i=1}^{N}\sum_{j=1}^{N} \left\{ [\widehat{\mathrm{Std}}(m_{0i})]^2 + [\widehat{\mathrm{Std}}(m_{0j})]^2 + \sigma^2 \right\} + \sum_{i=1}^{N} \left\{ [\widehat{\mathrm{Std}}(m_{0i})]^2 + [\widehat{\mathrm{Std}}(m_{0i})]^2 + \sigma^2 \right\} \right)^{\frac{1}{2}}. \tag{4.69}$$

The summations in this expression can be performed separately, so $\|\Delta\mathbf{C}\|_F$ can be rewritten to

$$\begin{aligned}
\mathrm{E}[\|\Delta\mathbf{C}\|_F] &\approx \frac{\sigma}{\sqrt{K}} \left(\sum_{i=1}^{N}\sum_{j=1}^{N} \left\{ [\widehat{\mathrm{Std}}(m_{0i})]^2 + [\widehat{\mathrm{Std}}(m_{0j})]^2 + \sigma^2 \right\} + \sum_{i=1}^{N} \left\{ [\widehat{\mathrm{Std}}(m_{0i})]^2 + [\widehat{\mathrm{Std}}(m_{0i})]^2 + \sigma^2 \right\} \right)^{\frac{1}{2}} \\
&= \frac{\sigma}{\sqrt{K}} \left(\sum_{i=1}^{N}\sum_{j=1}^{N} [\widehat{\mathrm{Std}}(m_{0i})]^2 + \sum_{i=1}^{N}\sum_{j=1}^{N} [\widehat{\mathrm{Std}}(m_{0j})]^2 + \sum_{i=1}^{N}\sum_{j=1}^{N} \sigma^2 + \sum_{i=1}^{N} [\widehat{\mathrm{Std}}(m_{0i})]^2 + \sum_{i=1}^{N} [\widehat{\mathrm{Std}}(m_{0i})]^2 + \sum_{i=1}^{N} \sigma^2 \right)^{\frac{1}{2}} \\
&= \frac{\sigma}{\sqrt{K}} \left(N\sum_{i=1}^{N} [\widehat{\mathrm{Std}}(m_{0i})]^2 + N\sum_{j=1}^{N} [\widehat{\mathrm{Std}}(m_{0j})]^2 + N^2\sigma^2 + \sum_{i=1}^{N} [\widehat{\mathrm{Std}}(m_{0i})]^2 + \sum_{i=1}^{N} [\widehat{\mathrm{Std}}(m_{0i})]^2 + N\sigma^2 \right)^{\frac{1}{2}} \\
&= \sigma \sqrt{\frac{N+1}{K} \left[2\sum_{i=1}^{N} \left\{ [\widehat{\mathrm{Std}}(m_{0i})]^2 \right\} + N\sigma^2 \right]}.
\end{aligned} \tag{4.70}$$

Substituting (4.63) into this equation and defining the signal to noise ratio (in agreement with Section 4.2.2) as

$$\mathrm{SNR} = \frac{\rho^2 \|\mathbf{h}\|_F^2}{N\sigma^2} \tag{4.71}$$

we get

$$\begin{aligned}
\mathrm{E}[\|\Delta\mathbf{C}\|_F] &\approx \sigma\sqrt{\frac{N+1}{K}\left[2\sum_{i=1}^{N}\{[\widehat{\mathrm{Std}}(m_{0i})]^2\}+N\sigma^2\right]} \\
&= \sigma\sqrt{\frac{N+1}{K}\left[2\sum_{i=1}^{N}\{\rho^2\mathbf{h}_i^2\}+N\sigma^2\right]} \\
&= \sigma\sqrt{\frac{N+1}{K}\left[2\rho^2\|\mathbf{h}\|_F^2+N\sigma^2\right]} \\
&= \sigma\sqrt{\frac{N+1}{K}[2N\sigma^2\,\mathrm{SNR}+N\sigma^2]} \\
&= \sigma\sqrt{\frac{N(N+1)\sigma^2}{K}[2\,\mathrm{SNR}+1]} \\
&= \sigma^2\sqrt{N(N+1)\frac{[2\,\mathrm{SNR}+1]}{K}}. \qquad (4.72)
\end{aligned}$$

For large $N \gg 1$ the limit reduces to

$$\begin{aligned}
\mathrm{E}[\|\Delta\mathbf{C}\|_F] &\approx \sigma^2\sqrt{N^2\frac{2\,\mathrm{SNR}+1}{K}} \\
&= \sigma^2 N\sqrt{\frac{2\,\mathrm{SNR}+1}{K}}. \qquad (4.73)
\end{aligned}$$

This formula gives a simple expression of the expected Frobenius norm of the error of the covariance matrix. It shows the dependence of the covariance estimation error on different parameters and their interplay, i.e. the influence of the signal to noise ratio SNR, the number of EEG/MEG channels N and the number of samples K used for the covariance estimation.

Interestingly, the covariance matrix error for example increases with the SNR, but the relative covariance error $\frac{\|\Delta\mathbf{C}\|_F}{\mathrm{SNR}}$ decreases because

$$\frac{\|\Delta\mathbf{C}\|_F}{\mathrm{SNR}} \approx \frac{\sigma^2 N\sqrt{\frac{2\,\mathrm{SNR}+1}{K}}}{\mathrm{SNR}} \sim \frac{\sqrt{\mathrm{SNR}}}{\mathrm{SNR}} = \frac{1}{\sqrt{\mathrm{SNR}}}. \qquad (4.74)$$

Increasing sensor noise will obviously also increase the covariance error and so will an increasing number of channels N. Increasing the number of sample points in contrast will lead to a smaller covariance matrix error, which is consistent with the assumption that in the limit of infinite integration the covariance matrix is determined correctly, hence without any error.

At this point Brookes et al. [6] argue that according to the sampling theorem equation (4.73) only applies to unfiltered data, i.e. in the case where the signal bandwidth (δf) is at the Nyquist limit, i.e. $\delta f = \tau/2$, where τ is the sampling

frequency. This would mean that only in this case K would be the number of useful samples. If the bandwidth was reduced by filtering, the number of 'useful' samples that could be recorded during the time window t_{cov} would be

$$K_{\mathrm{useful}} = 2t_{\mathrm{cov}}\delta f. \tag{4.75}$$

K_{useful} can be thought of as a measure of how much information is contained in the data. In this context Brookes et al. suggest that in the case where $\delta f < \tau/2$ holds, (4.73) should be rewritten to [6]

$$\|\Delta\mathbf{C}\|_F \approx \sigma^2 N\sqrt{\frac{2\,\mathrm{SNR}+1}{2t_{\mathrm{cov}}\delta f}}. \tag{4.76}$$

However, the application of the sampling theorem in the situation described above is not appropriate, as the sampling theorem is based upon the cutoff frequency Δf, rather than the bandwidth δf. The application of the sampling theorem is also problematic, as it exploits the determinisic character of the signal, but the former derivations are based on random processes as discussed in [6]. Although the derivation given in [6] does not hold, for recorded data that is entirely due to noise equation (4.75) can still be derived differently:
A signal recorded with sampling frequency τ over a time interval with the length t_{cov} has a cutoff frequency Δf of

$$\Delta f = \frac{1}{2\tau}, \tag{4.77}$$

hence

$$\frac{1}{\tau} = 2\Delta f. \tag{4.78}$$

The number of samples recorded is given by

$$K = \frac{t_{\mathrm{cov}}}{\tau}. \tag{4.79}$$

Together this yields

$$K = \frac{t_{\mathrm{cov}}}{\tau} = 2t_{\mathrm{cov}}\Delta f. \tag{4.80}$$

Gaussian noise by definition incorporates all frequencies within the Nyquist limit with the same probability. As we are aiming at estimating the source variance, it should be noticed that due to Parseval's Theorem we can estimate the variance in the Fourier space by applying the formula of the empirical variance (except for an unimportant factor). Therefore we will consider the Fourier transformed signal. Here we assume that the Fourier transformed samples are stochastically independent.

Applying a discrete Fourier transform to the K recorded samples gives K samples in the Fourier space ranging from $-\Delta f$ to Δf. Bandpass filtering would

remove all samples in the Fourier space but k samples within a frequency band δf ($-\delta f$ respectively) and the relationship

$$\frac{\delta f}{\Delta f} = \frac{k}{K} = \frac{k}{2t_{\text{cov}}\Delta f} \tag{4.81}$$

holds, which can be rewritten to

$$k = 2t_{\text{cov}}\delta f. \tag{4.82}$$

This k corresponds to the term K_{useful} used by Brookes et al. [6].

Note here that for equation (4.81) the assumption was used that the K samples in the Fourier space were uniformly distributed across all frequencies between $-\Delta f$ and Δf. In other words (4.75) and thereby (4.76) only hold for noise data and generally not for deterministic signals.

Brookes et al. present simulations to validate (4.76), but they only use band-pass filtered random samples as signals (as well as noise). This supports our derivation of (4.76), but does not hold for deterministic signals. A real brain signal consists of a deterministic part and noise. It is not clear to what extent (4.76) holds in such realistic situations.

However, the signal in the simulations in [6] has the same properties as noise. Therefore the simulations only support the validity of (4.76) for noise signals. In order to validate the effects of inappropriate covariance estimation in general it would be necessary to set up simulations where the brain source is represented by a deterministic signal.

5 Practical Application of Synthetic Aperture Magnetometry

In this chapter the influence of volume conductor properties on the SAM results will be examined. For this purpose synthetic data was simulated and analyzed by the beamformer (SAM) that was implemented as a part of the SimBio software (see Section 5.2.4). In the following a detailed description of the volume conductor model will be given, followed by some crucial implementation details. After that the simulations that were made will be presented and discussed.

5.1 The Finite Element Model

The FE model that was used for the beamformer analysis is the same model that was used and described in [57]. This model was built to take into account realistic head shapes as well as conductivity anisotropies in the skull.

The realistic head shape is reflected in the finite element mesh, which was derived from MRI data. As described in [57], T1-weighted MRI is well suited for the segmentation of tissue boundaries like white and grey matter, outer skull and skin. Proton density (PD) weighted MRI sequences are more successful in identifying the inner skull surface as the quantity of water protons between intracranial and bone tissues is large.

5.1.1 Measurement of T1- and PD-MRI

MR imaging of a healthy 32 year old male subject was performed on a 3 Tesla whole-body scanner (Medspec 30/100, Bruker, Ettlingen/Germany). For the T1-MRI, an inversion recovery MDEFT sequence [23] was employed (flip angle of 25°, $TR = 11.7$ ms, $TE = 6$ ms, $T_{MD} = 1.3$ s). For the 3D PD-MRI, acquired one week later, a 3D FLASH protocol [15] with $TE = 6$ ms, a flip angle of 25° and $TR = 11.7$ ms was used. The scan resolution was $1 \times 1 \times 1.5$ mm^3 in both acquisitions, which were linearly interpolated to an isotropic 1 mm^3 voxel size.

5.1.2 Registration and Segmentation

Constructing a realistic volume conductor model requires segmentation of the different tissues within the head with special attention to the poorly conducting

human skull [17, 10, 35, 20, 33].

In order to correct for different subject positions and geometrical distortions, T1- and PD-MRI were first aligned with a voxel-similarity based affine registration without pre-segmentation using a cost-function based on mutual information [55, 57]. The T1 images provided the information on soft tissues while the registered PD image enabled the segmentation of the inner skull surface.

Wolters et al. used a nearly automatic segmentation process consisting of a 3D implementation of an Adaptive Fuzzy C-Means classification method that compensates for image intensity inhomogeneities (based on the original work in two dimensions of [30]), followed by a deformable model algorithm to smooth the inner and outer skull surfaces [55]. Five head compartments were segmented out of the bimodal dataset; skin, skull, cerebrospinal fluid (CSF), grey and white matter. In source reconstruction, it is generally accepted that the weak volume currents outside the skull and far away from EEG and MEG sensors have a negligible influence on the measured fields [7]. Therefore, no effort was made to segment the face and instead a cutting procedure like that reported in standard boundary element head modelling was used (see e.g. [51]).

5.1.3 FE mesh generation

A prerequisite for FE modelling is the generation of a mesh that represents the geometric and electric properties of the head volume conductor. To generate the mesh, Wolters et al. [57] used the software CURRY[1] to create a surface-based tetrahedral tessellation of the five segmented compartments. The procedure exploits the Delaunay-criterion, enabling the generation of compact and regular tetrahedra, and is described in detail elsewhere [51, 55]. The process resulted in a finite element model with 147,287 nodes and 892,115 tetrahedra elements.

5.1.4 Finite Element Conductivity and Skull Tensor Eigenvalues

The finite elements were then labeled according to their compartment membership and assigned the following conductivities for the isotropic head model [14, 38, 19]: skin = 0.33 S/m, skull = 0.0042 S/m (skull to skin conductivity ratio of approximately 1:80) and brain = 0.33 S/m (the brain includes grey matter, white matter and CSF). The resulting FE mesh is shown in Figure 5.1[2]

The human skull shows a conductivity with high resistance in the radial direction (as a first approximation, a series connection of a high, a low and a high

[1] CURrent Reconstruction and Imaging, http://www.neuro.com.
[2] image created with TetView, http://tetgen.berlios.de/tetview.html

resistor for inner compacta, spongiosa and outer compacta) and much lower resistance in the tangential directions (parallel connection of the same three resistors) [38, 57].

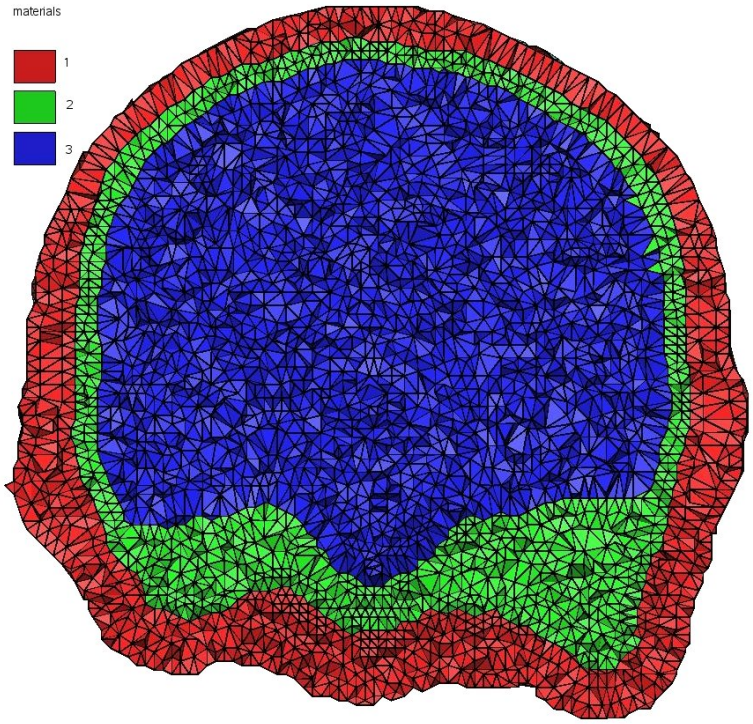

Figure 5.1: Axial cut through the realistically shaped FE model with elements coloured according to their compartment: red for skin, green for skull and blue for the brain.

Marin et al. have pointed out the importance of well-defined skull conductivity tensor eigenvectors by reporting errors in the simulated EEG for the case of an erroneous modelling [24]. Wolters et al. determined the radial direction from a strongly smoothed triangular mesh, which was shrunken from the outer skull onto the outer spongiosa surface using a discrete deformable surface model [55].

Realistic modelling of the conductivity tensor eigenvalues in the skull is a difficult task, not only because the absolute and relative thicknesses of spongiosa and compacta layers vary and their boundaries are difficult to segment, but especially because of inhomogeneous skull resistivity and an inter- and intrasubject variability which can be related to age, diseases, environmental factors, and personal constitution [38, 22, 19, 32, 28, 1]. Wolters et al. therefore started from the commonly used isotropic conductivity value of $\sigma_{skull} = 0.0042$ S/m [20, 10, 8, 51] and simulated the anisotropic case in the following way: For a given anisotropy ratio, $\sigma^{\mathrm{rad}} : \sigma^{\mathrm{tang}}$, radial and tangential eigenvalues were computed by obeying the *volume constraint* [55], which retains the geometric mean of the eigenvalues

and thus the volume of the conductivity tensor, i.e.

$$\frac{4}{3}\pi\sigma^{\mathrm{rad}}(\sigma^{\mathrm{tang}})^2 \stackrel{!}{=} \frac{4}{3}\pi\sigma^3_{\mathrm{skull}}. \tag{5.1}$$

According to [38, 11, 29, 48, 24], the skull has an anisotropy ratio of 1:10. Using the volume constraint, $\sigma^{\mathrm{rad}} = 0.000905$ and $\sigma^{\mathrm{tang}} = 0.00905$ were obtained.

5.1.5 3-layer Isotropic Sphere Model

The 3-layer isotropic sphere model was obtained by fitting a sphere to the realistic EEG sensor positions using the coordinate system of the according FE model. This sphere has a radius of 89.66 mm and represents the outer boundary of the head volume. The outer skull was then modeled by inserting a concentric sphere with radius 83.33 mm and the inner skull was modelled by adding another concentric sphere with radius 74.89 mm. Hence, the volume inside the innermost sphere represents the brain compartment. The electrode positions were gained by projecting the realistic sensor positions to the surface of the outer sphere.

5.2 Beamformer Application

In this section we will present practical applications of SAM to synthetic data. For this purpose crucial details of simulating synthetic data will be discussed followed by a close examination of the effects that volume conduction has on the SAM results.

5.2.1 Possible Source Locations

In order to examine the effects of volume conductor modelling on beamformer results, synthetic data must be produced. In particular this means that for a number of distinct source locations the sensor leadfield is computed using a certain volume conductor model. The question that implicitly arises is how to choose these distinct source locations.

As described in Section 2.3, brain source activity is usually located in the cortex of the human brain. Another issue that has to be taken into account is that the distributed source model used for the Venant approach and therefore also the forward solution is dependent on the FE mesh. As described in Section 3.6.3, the blurred dipole model distributes monopolar loads to neighbouring FE nodes. In our simulations we only want to take source locations into account, where all monopolar loads are placed in the cortex sheet. This property will be called the Venant property. It makes sure that all neighbouring finite elements represent the same tissue conductivity.

To identify locations that incorporate the requirements described above, we started off by distributing a $2 \times 2 \times 2$ mm source-mesh across grey- and white

matter of a segmented 5-layer (skin, skull, CSF, grey matter, white matter) MR image with resolution $1 \times 1 \times 1$ mm. All the nodes of this mesh were examined with regard to the Venant property. For this purpose each node of the source mesh was projected to his nearest neighbour in the FE mesh. If this nearest neighbour and all of his neighbouring FE nodes had the conductivity of the brain, the according source node was labeled to fulfil the Venant property, otherwise it was not.

The next step was to resample the segmented MR image to have a resolution of $2 \times 2 \times 2$ mm using nearest neighbour interpolation to determine the values of the enlarged voxels. The voxel positions of the grey- and white matter segments were now a subset of the source-mesh nodes. Distance transformation with respect to the white matter compartment was performed and all voxels with a distance smaller or equal to 2 mm were added to the white compartment. This can be thought of as a slightly blown up white matter compartment. We were now seeking to extract the surface of this blown up white matter compartment which will lie within the grey matter. This was done with the use of a morphologic operator. An erosion was performed on the surface of the enlarged white matter compartment and the removed voxels are the very candidates for source locations

As mentioned above, these voxels can be identified with nodes of the source-mesh. The last step was to remove all candidates whose corresponding nodes did not fulfil the Venant property, which had been checked previously. The final result is a number of possible source locations that are all located in the cortex and fulfil the Venant property. These locations are shown in Figure 5.2.

5.2.2 Beamformer Resolution and Noise

In order to investigate the effect of volume conductor modelling on beamformer results, synthetic data is used as this provides the possibility of examining certain aspects in a clean environment. When a single source is simulated using an arbitrary volume conductor, then in the absence of noise, the beamformer reconstruction using the same volume conductor produces a sharp peak at the original source position. A very sharp peak indicates that even sources with a different but very similar leadfield are blocked. This has been validated using a realistically shaped 3-layer isotropic FE model and the result is shown in Figure 5.3 a).

The purpose of this work is to investigate the influence of the head model on the SAM reconstruction result. Therefore, the model used for the reconstruction is usually not the same one as that used for the simulation of the data. In these cases the very high resolution that was obtained in the absence of noise is a serious problem as the leadfields that are computed for the nodes of the search space grid in the reconstruction model may significantly differ from the reference leadfield. In this context it becomes necessary to decrease the resolution of the beamformer, which results in broader peaks.

One way to achieve this is to add noise to the simulated data. In order to

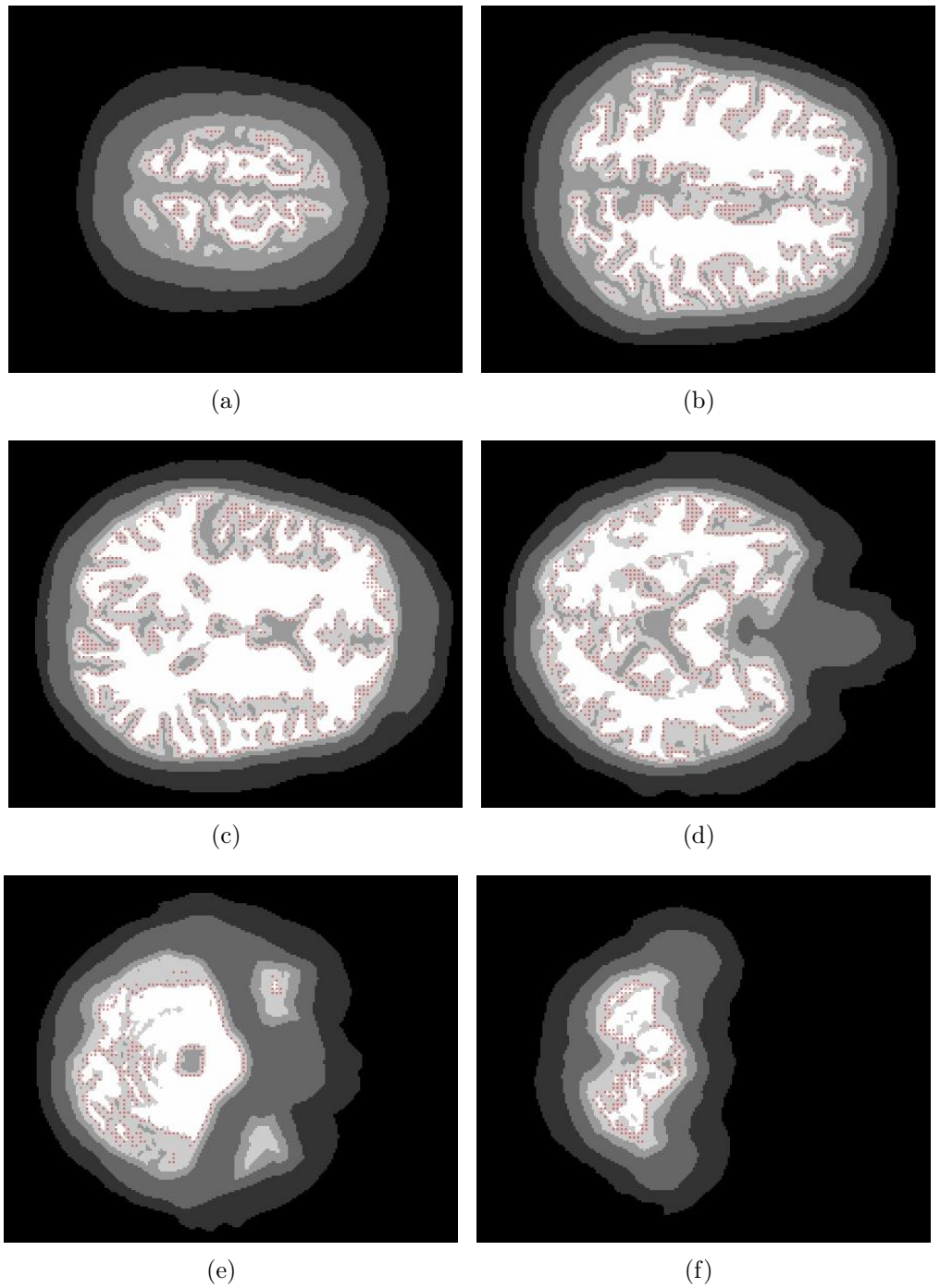

(a) (b)

(c) (d)

(e) (f)

Figure 5.2: Selection of sagittal MR slices with red dots indicating the source locations used for simulations. (a)-(f) ordered from superior to inferior.

avoid errors due to finite integration times (see Section 4.4) we do not generate noise by random numbers but rather use the theoretical covariance matrix of the form $\mathbf{C}_\Sigma = \sigma^2\mathbf{I}$. Here σ^2 represents the noise level. Under the assumption that the noise and the signal are uncorrelated, the data covariance matrix that is used to compute the beamformer weight can be written as

$$\mathbf{C} = \mathbf{C}_{\text{signal}} + \mathbf{C}_\Sigma = \mathbf{C}_{\text{signal}} + \sigma^2\mathbf{I}, \tag{5.2}$$

where $\mathbf{C}_{\text{signal}}$ represents the covariance matrix of the noise free simulated data. Figure 5.3 shows plots of the beamformer resolution obtained using different noise levels. Again the realistically shaped 3-layer isotropic FE model was used or the simulation as well as for the reconstruction. As expected, an increase of noise results in a decrease of resolution. The plots in Figure 5.3 all represent pseudo-Z values of the beamformer output, i.e. the SAM results were normalized by the beamformer projected sensor noise. However, the effect of noise blurring the beamformer peaks would also apply to the beamformer output before computing the pseudo-Z value. In spite of broadening the peaks the beamformer maximum peak will still be found at exactly the same position as the sharp peak.

The introduction of noise to simulated data does not only broaden the peaks, it also causes artifacts which are presented in Figure 5.4. The small light spots in the SAM reconstruction have a much higher absolute value than the peak value at the original position of the simulated source. These artifacts are due to the noise that was added to the simulated data. The beamformer projected noise at a position $\mathbf{q}$ is given by

$$\mathbf{w}^T(\mathbf{q})\mathbf{C}_\Sigma\mathbf{w}(\mathbf{q}) = \mathbf{w}^T(\mathbf{q})\sigma^2\mathbf{I}\mathbf{w}(\mathbf{q}) = \sigma^2\|\mathbf{w}(\mathbf{q})\|, \tag{5.3}$$

Using (4.34) it can be seen that the projected noise typically increases with decreasing leadfield length:

$$\mathbf{w}^T(\mathbf{q})\mathbf{C}_\Sigma\mathbf{w}(\mathbf{q}) \sim \frac{1}{\|\mathbf{h}(\mathbf{q})\|} \tag{5.4}$$

We have validated that the artefacts in Figure 5.4 are right at those positions where the length of the leadfield is comparably small, hence at positions where $\frac{1}{\|\mathbf{h}(\mathbf{q})\|}$ is large.

A possible and recommendable way of dealing with these artefacts is to use pseudo-Z values that are gained by dividing the beamformer output by the beamformer projected noise. This will compensate for the artefacts while the peak at the reconstructed source position becomes sharper, but remains visible as shown in Figure 5.4.

5.2.3 Source Orientation

For each source location $\mathbf{q}$ the dipole orientation that would maximize the expected localization error was determined. Therefore, the leadfield for the forward

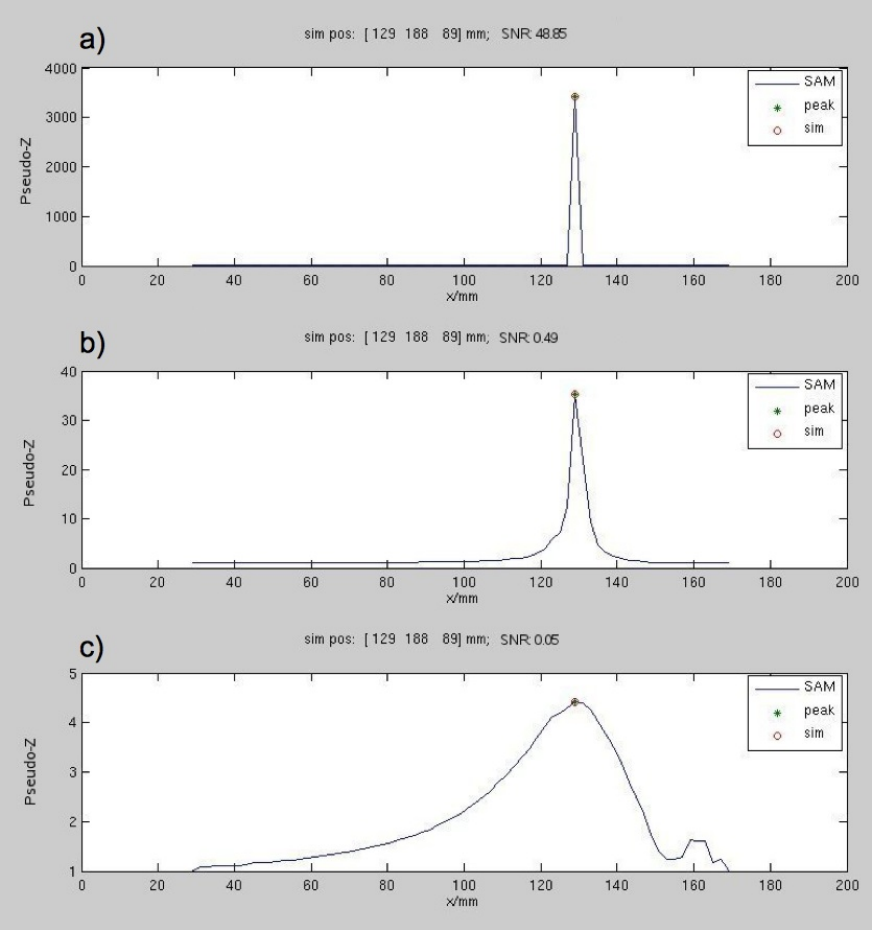

Figure 5.3: Plots of the beamformer resolution along the x-achses (right to left) for different noise levels (pseudo-Z values). The red circles indicate the true location of the simulated source, the green star represents the maximum peak of the SAM reconstruction.

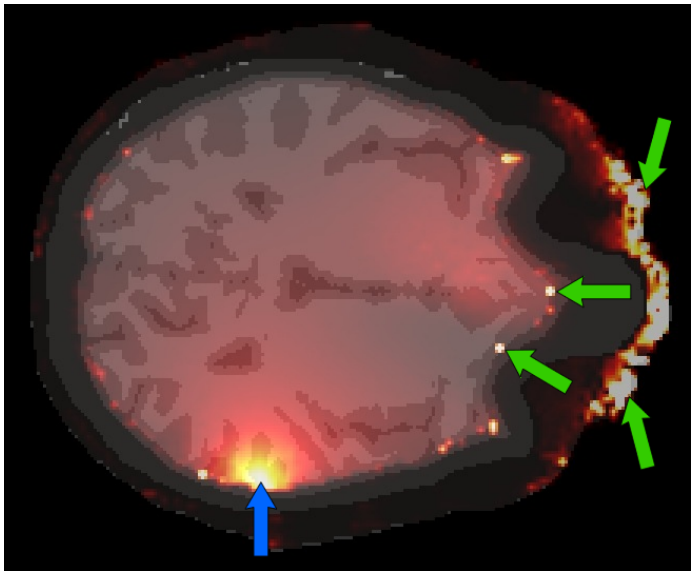

(a)

(b)

Figure 5.4: (a) SAM reconstruction results before applying pseudo-Z correction for projected noise. The blue arrow points to the true source location, the green arrows point at some arbitrary artefacts. (b) SAM reconstruction using pseudo-Z values to compensate for artefacts due to sensor noise. The blue arrow points at the correctly reconstructed source postion.

model $\mathbf{H}^{\text{sim}}(\mathbf{q})$ and the leadfield for the inverse model $\mathbf{H}^{\text{sam}}(\mathbf{q})$ were computed. For the difference in these leadfields $(\mathbf{H}^{\text{sim}}(\mathbf{q}) - \mathbf{H}^{\text{sam}}(\mathbf{q}))$ a singular value decomposition (SVD) was performed. The dipole orientation was chosen to have the direction of the eigenvector to the largest eigenvalue of the SVD. In this direction the L^2 norm of the potential difference between forward and inverse model is maximized. Choosing this dipole orientation, we expect to find localization errors close to the largest localization errors that can be observed for any dipole at location $\mathbf{q}$.

5.2.4 Simulation Software

All simulations presented in this thesis have been run using the SimBio[3] software package.

The SimBio code provides algorithms to solve the EEG/MEG inverse problem as well as analytical and quasi analytical solutions to the forward problem in multilayer sphere models. In addition there are Boundary Element Method (BEM) solutions for the forward problem in realistically shaped multilayer isotropic head models.

SimBio allows the generation of EEG and MEG forward solutions based on the Finite Element method. The SAM implementation used for the inverse solutions was embedded into SimBio. The iterative forward calculations and SAM reconstructions were realized by a MATLAB®[4] routine, calling the according SimBio functions.

The visualizations of the results were done with SCIRun[5] and MRIcro[6], the SAM results generated by the SimBio software were processed with MATLAB® to generate appropriate input files for SCIRun and MRIcro.

5.2.5 Forward Simulation and SAM Reconstruction

After identifying possible source locations and determining the source orientation for each location, a forward simulation was performed separately for each of these sources. The source time course was simulated as a sine wave with a frequency of 40 Hz and an amplitude of 10 nAm. The sampling frequency was set to 1200 Hz and 100 trials with 200 samples per trial were simulated. The EEG sensors were arranged according to the 10-20 system. Their positions relative to the head model are shown in Figure 5.5.

The simulated measurements were used to construct the noise free data covariance matrix $\mathbf{C}_{\text{signal}}$. Perfect noise at a level of $\sigma^2 = 2 \cdot 10^{-13}$ V was simulated by adding the noise covariance matrix $\mathbf{C}_\Sigma = \sigma^2 \mathbf{I}$ to $\mathbf{C}_{\text{signal}}$. The resulting covariance matrix $\mathbf{C} = \mathbf{C}_{\text{signal}} + \mathbf{C}_\Sigma$ was used to compute the SAM filter weights.

[3] https://www.mrt.uni-jena.de/neurofem/index.php/Main_Page
[4] http://www.mathworks.de/products/matlab/
[5] http://software.sci.utah.edu/scirun.html
[6] http://www.sph.sc.edu/comd/rorden/mricro.html

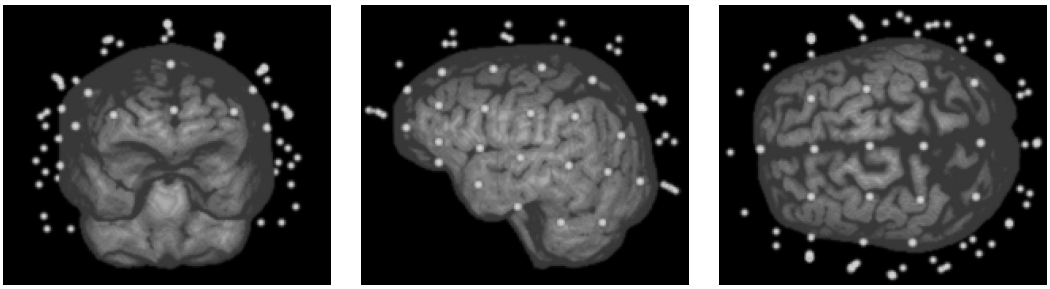

(a) axial view (b) sagittal view (c) coronal view

Figure 5.5: Sensor locations relative to the brain.

As we are interested in the influence of volume conductor modelling on the beamformer results, two scenarios will be analyzed in particular:

- The first scenario we will focus on incorporates a forward simulation in the realistically shaped 3-layer isotropic FE model and a SAM reconstruction on the basis of a 3-layer isotropic sphere model. The idea of analyzing this experimental setup is to reveal effects that are entirely due to the differences in geometry between the forward model (realistic shape) and the inverse model (sphere).

- The second scenario consists of a forward simulation in the realistically shaped 3-layer anisotropic FE model followed by a SAM reconstruction using the realistically shaped 3-layer isotropic FE model. This analysis is supposed to show up the pure skull anisotropy effect.

5.2.6 The Geometry Effect

As described in Section 5.2.5, the geometry effect was examined by simulating single dipoles in the realistically shaped 3-layer isotropic FE model and performing a SAM reconstruction on the basis of a 3-layer isotropic sphere model. The differences between the original source position and the reconstructed source position are visualized in Figure 5.6. Note that the displacement cones in that figure do not each represent a single dipole but the average over all displacement cones within a volume of 1cm^3. The average was computed by dividing the source space into 1 cm^3 cubes and determining the arithmetic mean of all source positions within one cube first. This average source position was chosen as the origin of the corresponding cone. The direction and length were then determined by calculating the arithmetic mean of all the displacement vectors (reconstructed position - true source location) to the sources within that voxel. The colours encode the lengths of the cones in mm, i.e. the average displacement within the represented voxels.

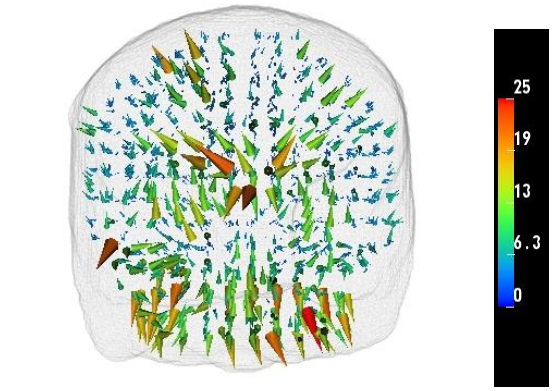

(a) axial view

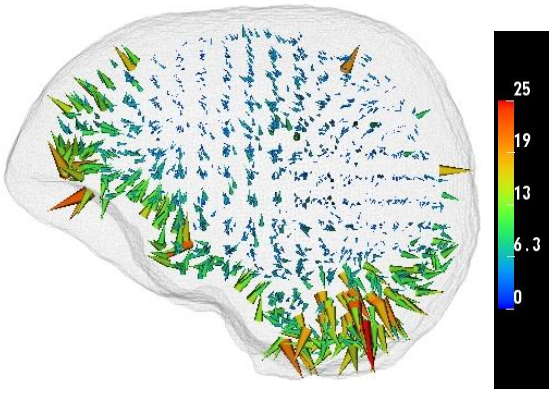

(b) sagittal view

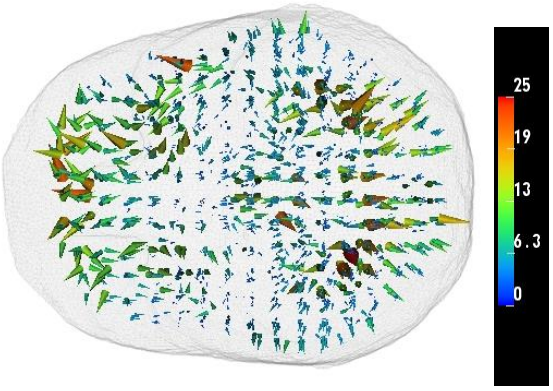

(c) coronal view

Figure 5.6: The geometry effect (isotropic FEM vs. isotropic sphere model). Cones pointing from the true source location to the reconstructed position. Each cone represents the average of all displacement vectors within a voxel of 1 cm^3.

The results in Figure 5.6 clearly show large reconstruction errors in the prefrontal cortical (PFC) areas that we are especially interested in. The sources are 'pushed' inside or outside the head depending on under- or over-estimation of the skull thickness. Even bigger errors are found in the regions around the brainstem and the cerebellum. These results correspond well with the geometrical differences between the realistic head shape and the sphere, which are shown in Figure 5.7 and Figure 5.8. In Figure 5.7 the distance of the head surface to the sphere surface was estimated for each FE skin surface node by computing the RMS distance to the sphere surface over all FE skin surface nodes within a radius of 1 cm. Figure 5.8 shows an overlay of the segmented MR image and the Sphere model. Comparing this to Figure 5.6 it can clearly be seen that the reconstruction errors become large in exactly those areas where the sphere fits the head shape badly. The large errors in the brainstem and the cerebellum may as well be partly due to the bad sensor coverage in these areas, which is presented in Figure 5.5 and Figure 5.7.

The results gained from these simulations stand in close agreement with various publications on the geometry effect. Hämäläinen and Sarvas [18] compared the MEG forward solutions of sphere models to the MEG forward solutions of realistically shaped isotropic head models and found considerabel differences, especially in frontal areas. Van Uitert and Johnson [45] have produced synthetic MEG data using a 5-layer isotropic FE model and performed inverse calculations based on 5 different sphere models. The overall outcome of their study was, that localization errors for deep sources were generally larger than the localization error for superficial sources that were located closer to the sensors. Van Uitert et al. also pointed out differences in the MEG forward solutions of realistically shaped head models and sphere models in [46].

5.2.7 The Anisotropy Effect

In order to investigate the anisotropy effect a number of sources were simulated separately in the realistically shaped 3-layer anisotropic FE model and then reconstructed with the realistically shaped 3-layer isotropic FE model. The results are shown in Figure 5.9. Again the cones represent the average reconstruction error across all sources simulated within 1 cm^3 voxels. The average was determined analogously to the averaging process described for the visualization of the geometry effect in Section 5.2.6. As above, the colours encode the lengths of the cones in mm, i.e. the average displacement within the represented voxels.

The simulation results in Figure 5.9 show that by disregarding the anisotropy of the skull (here modeled as 1:10 (radial:tangential) following the volume constraint) leads to 'pushing' the sources further into the head.
This again confirms results that were presented by Marin et al. who investigated reconstruction errors when disregarding skull anisotropy [24]. As reported and validated in a sensitivity study by Huiskamp et al. correct modelling of the thickness of the skull is of high importance [20]. This means that in areas where

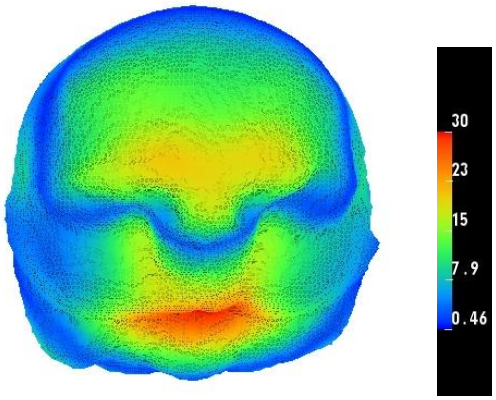

(a) axial view

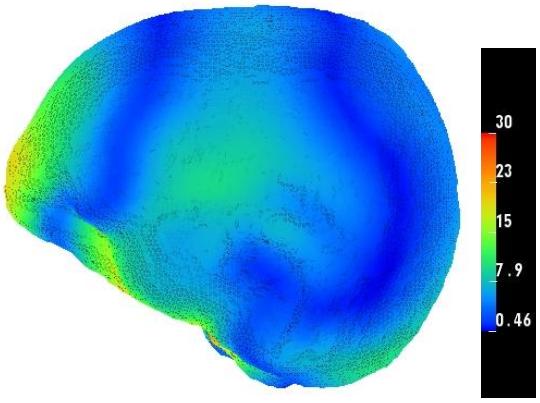

(b) sagittal view

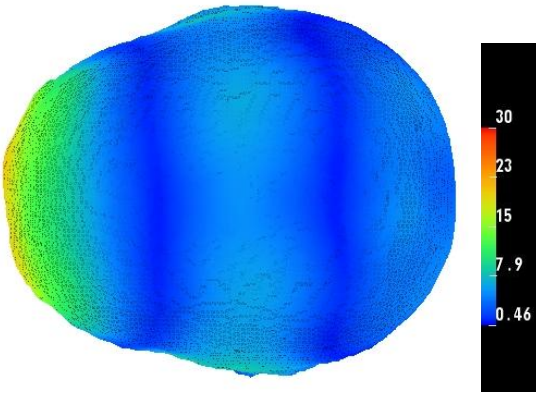

(c) coronal view

Figure 5.7: Differences between the sphere model and the realistically shaped FE model by means of the local mean square distance between the realistic head surface and the corresponding sphere's surface.

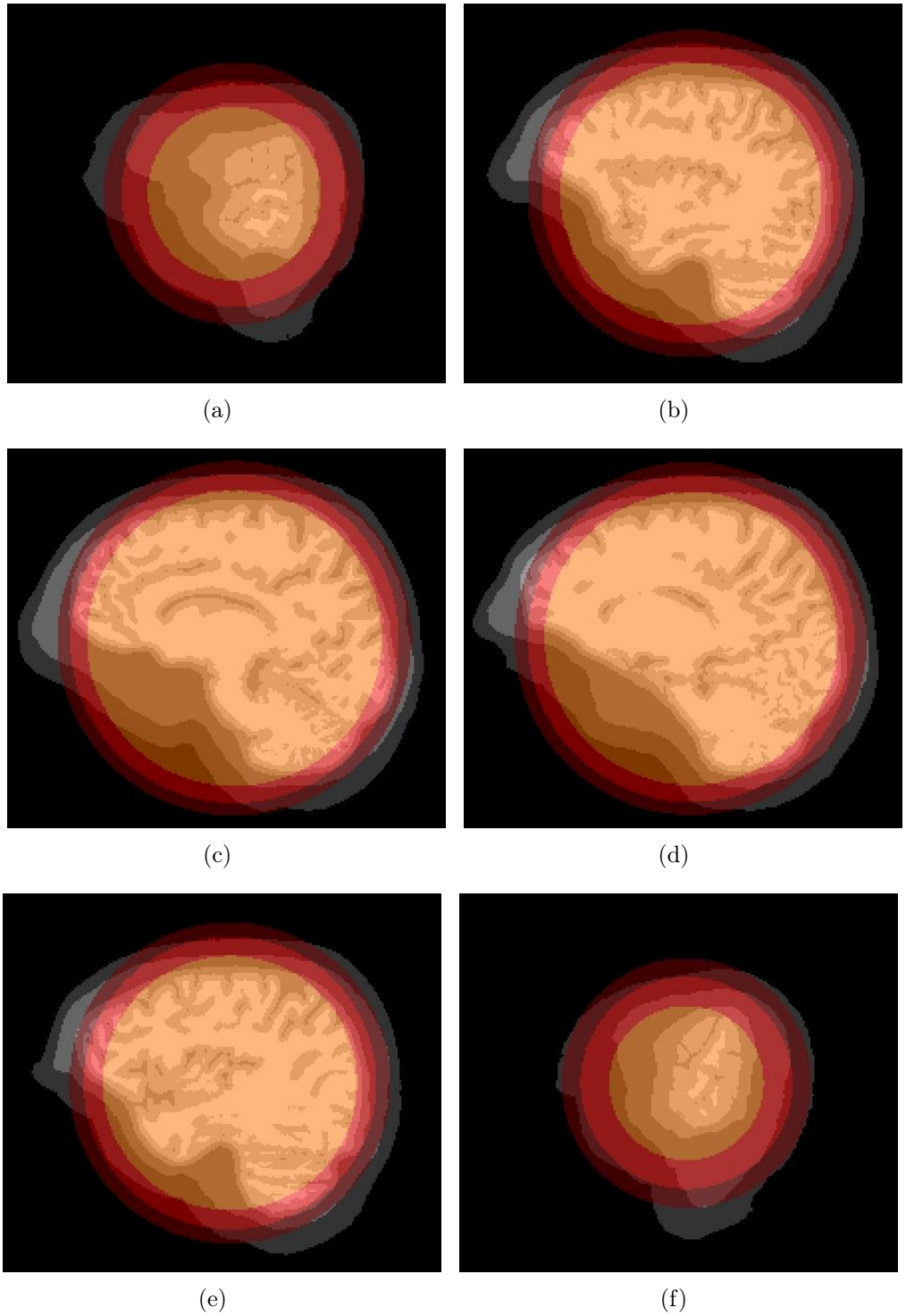

(a) (b)

(c) (d)

(e) (f)

Figure 5.8: (a)-(f): Selection of slices along the x-axes (ordered from right to left) showing an overlay of the MR that the realistically shaped 3-layer isotropic FE model was based on and the 3-layer sphere model.

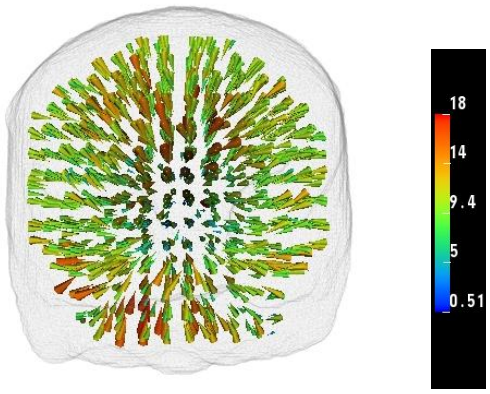

(a) axial view

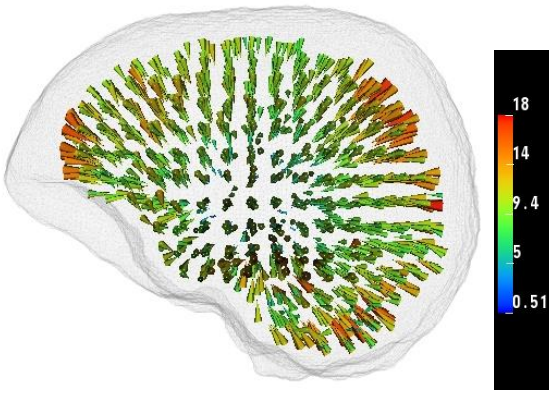

(b) sagittal view

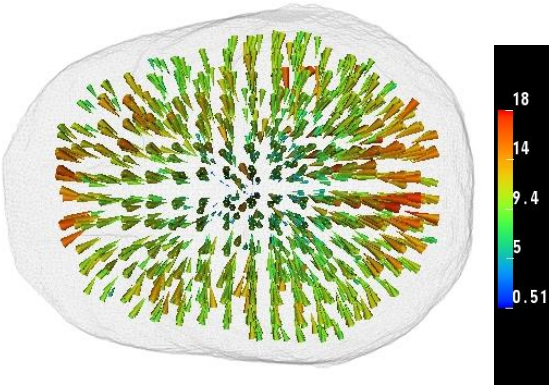

(c) coronal view

Figure 5.9: The anisotropy effect. Cones pointing from the true source location to the reconstructed position. Each cone represents the average of all displacement vectors within a voxel of 1 cm^3.

the skull is thick, the reconstruction error will be larger than in areas where the skull is rather thin. This is also observed in Figure 5.9 when comparing it to the thickness of the skull presented in Figure 5.10. We currently believe that, according to the global sensitivity study of Vallaghé et al. [47], the main effect is due to the change in radial skull conductivity by means of the volume constraint.

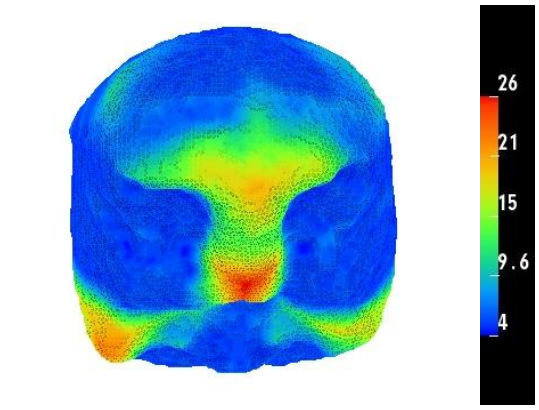

(a) axial view

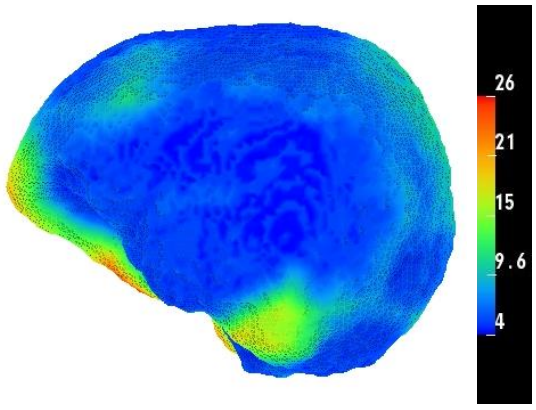

(b) sagittal view

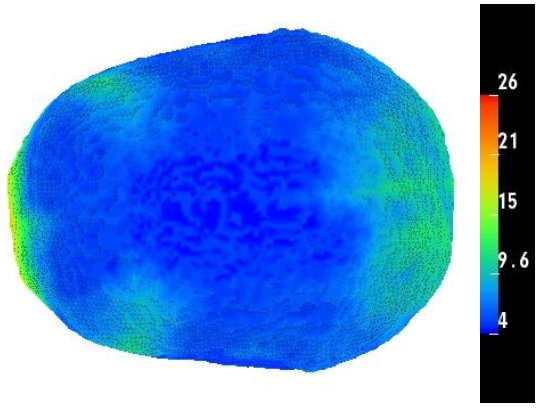

(c) coronal view

Figure 5.10: Thickness of the skull computed for each skull-skin boundary FE node as the distance to the closest CSF-skull boundary FE node.

6 Conclusion

The aim of this thesis was to investigate the influence of volume conduction on EEG beamformer analysis. For this purpose the forward problem and the underlying neural concepts were described. This was followed by a chapter on solving the associated inverse problem using beamformer techniques. These theoretical derivations provided the basis for the simulations performed in Chapter 5. The geometry effect between a 3-layer isotropic sphere model and a realistically shaped 3-layer isotropic FE-model, as well as the skull anisotropy effect in comparison of a realistically shaped 3-layer anisotropic FE-model and a realistically shaped 3-layer isotropic FE-model were examined in detail.

It was found that the geometry effect was especially large in those areas where the sphere model differed the most from the realistic head geometry. This included the PFC areas that were of high interest with respect to future real data studies as they were described in the introduction (anxiety disorders and sensory gating in schizophrenic diseases). For positions in the prefrontal cortex localization errors of up to 20 mm can be observed in Figure 5.6. Our results correspond well with other studies on the geometry effect that can be found in literature ([18, 20]).

The results presented for the anisotropy effect show that skull-anisotropy has a common effect on source localization across the whole head volume as all sources are pushed' into the head. The reconstruction errors appear to be larger in areas where the skull is thick than in areas where the skull is rather thin. This is especially the case in the prefrontal cortex. These results are again in close agreement with literature on the effect of skull-anisotropy ([57]). It however seems that the change in radial conductivity has a considerable influence [47].

Concludingly one can say that the geometry effect as well as the anisotropy effect do have significant influence on beamformer source analysis in 3-layer head models. Therefore it is recommended to use a realistically shaped head model that takes skull anisotropy into account for real data analysis, as this comes closest to the reality among those models that were discussed in this thesis.

7 Outlook

For the investigation of the effects of volume conduction on EEG beamformer analysis, this theses focused on 3-layer models as they are well suitable to examine the geometry effect and the anisotropy effect separately.

An effect that is still to be evaluated is the dependence of the beamformer results on the sensor coverage. As it was shown in Figure 5.5, the sensor coverage is only restricted to realistic EEG sensor positions. When working on synthetic data, as it was done throughout this thesis, it is also possible to place virtual sensors for example inside the neck in order to gain better coverage for sources near the brainstem or in the cerebellum.

The anisotropy effect has so far been observed for the volume constraint. A study incorporating the same radial skull conductivity as in the isotropic model but by a factor 10 higher tangetial skull conductivity may as well provide a deeper insight into the effects of skull anisotropy [21, 24, 47].

Another scenario that should be examined is to validate the simulations in this thesis that were all done for the EEG by performing the same simulation setup for the MEG. Combined EEG and MEG is of great interest.

In future work, an examination of 4- and 5-layer models may give further clues on volume conduction effects in beamformer source analysis. Using 5-layer models can also account for white matter conductivity anisotropy which might have an influence on the beamformer reconstruction results. It is expected that the deeper the source, the more important white matter anisotropy modelling is [57, 36]

And last but not least an application to real measured data should be the aim of future research. As described in the introduction, source reconstruction methods serve to actually learn more about the human brain, its functions and how it processes stimuli. Therefore the efficiency of a head model in combination with an inverse method should be judged by the applicability to real data problems.

List of Figures

Symbols

Symbol	Explanation
$\mathbf{A}$	upper case boldface symbols: vector fields or matrices depending on the context
$\mathbf{v}$	lower case boldface symbols: vectors unless indicated differently
$\delta(\cdot)$	Dirac δ-distribution
$\nabla \cdot \mathbf{A}$	Divergence of the vector field $\mathbf{A}$
$\times \mathbf{A}$	Curl of the vector field $\mathbf{A}$
$\nabla \Phi$	Gradient of a scalar potential Φ
Δ	Laplace Operator
$\langle \mathbf{a}, \mathbf{b} \rangle$	Scalar product of the vectors $\mathbf{a}$ and $\mathbf{b}$
$H^1(\Omega)$	Sobolev space over Ω
$L^2(\Omega)$	Space of square integrable functions over Ω
$L^\infty(\Omega)$	Space of essentially bounded functions over Ω
$C^2(\Omega)$	Space of twice continuously differentiable functions over Ω
$C^1(\Omega)$	Space of continuously differentiable functions over Ω
$C^0(\Omega)$	Space of continuous functions over Ω
$DIAG(n_1, \ldots, n_k)$	$k \times k$ Matrix with diagonal entries n_1 to n_k and all non-diagonal entries are zero
$\mathbf{A}^T$	Transpose of the matrix $\mathbf{A}$
$\mathbf{A}^{-1}$	Inverse of the matrix $\mathbf{A}$
$tr\{\mathbf{A}\}$	Trace of the matrix $\mathbf{A}$
$\mathrm{E}\{X\}$	Expected value of random quantity X
$\mathrm{Cov}(X, Y)$	Covariance of random quantities X and Y
$\mathrm{Cov}(X)$	Autocovariance of random quantity X
$\mathrm{Var}(X)$	Variance of random quantity X
$\mathrm{Std}(X)$	Standard deviation of random quantity X
$\| \cdot \|_F$	Frobenius norm

Bibliography

[1] M. Akhtari, H. Bryant, A. Marmelak, E. Flynn, L. Heller, J. Shih, M. Mandelkern, A. Matlachov, D. Ranken, E. Best, M. Di Mauro, R. Lee, and W. Sutherling. Conductivities of three-layer live human skull. *Brain Topography*, 14(3):151–167, 2002.

[2] W. Andrä and H. Nowak. *Magnetism in medicine – a handbook*. Wiley-VCH, Berlin, Weinheim, New York, Chichester, Brisbane, Singapore, Toronto, 1998.

[3] J. Bendat and A. Piersol. *Random Data: Analysis and Measurement Procedures*. John Wiley and Sons, New York, second edition, 1986.

[4] O. Bertrand, M. Thévenet, and F. Perrin. 3D finite element method in brain electrical activity studies. In J. Nenonen, H.M. Rajala, and T. Katila, editors, *Biomagnetic Localization and 3D Modelling*, pages 154–171. Report of the Dep. of Tech.Physics, Helsinki University of Technology, 1991.

[5] D. Braess. *Finite Elemente. Theorie, schnelle Löser und Anwendungen in der Elastizitätstheorie*. Springer, Berlin, 1997.

[6] M. Brookes, J. Vrba, S. Robinson, C. Stevenson, A. Peters, G. Barnes, A. Hillebrand, and P. Morris. Optimizing experimental design for meg beamformer imaging. *NeuroImage*, 39:1788–1802, 2008.

[7] P. Bruno, F. Vatta, S. Minimel, and P. Inchingolo. Referenced EEG and head volume conductor model: Geometry and parametrical setting. In *Proceedings of the 26th Annual International Conference IEEE Engineering in Medicine and Biology Society, San Francisco, USA, Sep. 1-5, http://www.ucsfresno.edu/embs2004*, 2004.

[8] H. Buchner, G. Knoll, M. Fuchs, A. Rienäcker, R. Beckmann, M. Wagner, J. Silny, and J. Pesch. Inverse Localization of Electric Dipole Current Sources in Finite Element Models of the Human Head. *Electroenc. and Clin. Neurophysiol.*, pages 267–278, 1997.

[9] M. Burger. *Skriptum zur Vorlesung: Numerik partieller Differentialgleichungen, Wintersemester 2006/07*. Institut für Numerische und Angewandte Mathematik, Westfälische Wilhelms-Universität Münster, 2007.

[10] B. Cuffin. Eeg localization accuracy improvements using realistically shaped head models. *IEEE Transactions on Biomedical Engineering*, 43:299–303, 1996.

[11] J. de Munck. The potential distribution in a layered anisotropic spheroidal volume conductor. *Journal of Applied Physics*, 64:465–469, 1988.

[12] J. de Munck, B. van Dijk, and H. Spekreijse. Mathematical dipoles are adequate to describe realistic generators of human brain activity. *IEEE Transactions on Biomedical Engineering*, 35(11):960–966, 1988.

[13] M. Gazzaniga. *The new cognitive neurosciences*. The MIT Press, 2000.

[14] L. Geddes and L. Baker. The specific resistance of biological material. A compendium of data for the biomedical engineer and physiologist. *Medical and Biological Engineering and Computing*, 5(3):271–293, 1967.

[15] A. Haase, J. Frahm, D. Matthaei, W. Hänicke, and K.-D. Merboldt. Flash imaging rapid nmr imaging using low flip-angle pulses. *Journal of magnetic resonance*, 67, 1986.

[16] W. Hackbusch. *Theorie und Numerik elliptischer Differentialgleichungen*. Teubner Studienbücher, 1986.

[17] M. Hämäläinen and J. Sarvas. Feasibility of the homogeneous head model in the interpretation of neuromagnetic fields. *Phys. Med. Biol*, 32:91–97, 1987.

[18] M. Hämäläinen and J. Sarvas. Realistic conductivity geometry model of the human head for interpretation of neuromagnetic data. *IEEE Transactions on Biomedical Engineering*, 36:165–171, 1989.

[19] J. Haueisen. Methods of numerical field calculation for neuromagnetic source localization. In *Dissertation, ISBN 3-8265-1691-5, Shaker Verlag Gmbh*, pages 3–8265, 1996.

[20] G. Huiskamp, M. Vroeijenstijn, R. van Dijk, G. Wieneke, and A. van Huffelen. The need for correct realistic geometry in the inverse eeg problem. *IEEE Transactions on Biomedical Engineering*, 46(11):1281–1287, 1999.

[21] B. Lanfer. *Validation and comparison of realistic head modeling techniques and applicaton to combined E/MEG data*. Diploma Thesis in Physics. Institute of Applied Physics, University of Münster, 2007.

[22] S. Law. Thickness and resistivity variations over the upper surface of the human skull. *Brain Topography*, 2:99–109, 1993.

[23] J. Lee, M. Garwood, R. Menon, G. Adriany, P. Anderson, C. Truwit, and K. Ugurbil. High contrast and fast 3d magnetic resonance imaging at high fields. *Magnetic Resonance in Medicine*, 34:308–312, 1995.

[24] G. Marin, C. Guerin, S. Baillet, and L. Garnero. Influence of skull anisotropy for the forward and inverse problem in eeg: simulation studies using the fem on realistic head models. *Human Brain Mapping*, 6:250–269, 1998.

[25] W. Nolting. *Grundkurs: Theoretische Physik, Elektrodynamic*. Zimmermann-Neufang, Ulmen, 1992.

[26] P. Nunez. Localization of brain activity with electroencephalography. In *Advances in Neurology*, pages 39–65, 1990.

[27] Y. Okada. Neurogenesis of evoked magnetic fields. In *Biomagnetism*, pages 399–408. Plenum Press, 1983.

[28] J. Ollikainen, M. Vauhkonen, P. Karjalainen, and J. Kaipio. Effects of local skull inhomogeneities on eeg source estimation. *Medical Engineering & Physics*, 21:143–154, 1999.

[29] M. Peters and J. de Munck. The influence of model parameters on the inverse solution based on megs and eegs. *Acta Oto-Laryngologica*, pages 61–69, 1991.

[30] D. Pham and J. Prince. An adaptive fuzzy c-means algorithm for image segmentation in the presence of intensity inhomogeneities. *Pattern Recognition Letters*, 20:57–68, 1999.

[31] R. Plonsey and D. B. Heppner. Considerations of quasi-stationarity in electrophysiological systems. *Bulletin of Mathematical Biophysics*, 29:657–664, 1967.

[32] R. Pohlmeier, H. Buchner, G. Knoll, A. Rienäcker, R. Beckmann, and J. Pesch. The influence of skull-conductivity misspecification on inverse source localization in realistically shaped finite element head models. *Brain Topography*, 9(3):157–162, 1997.

[33] C. Ramon, P. Schimpf, J. Haueisen, M. Holmes, and A. Ishimaru. Role of soft bone, csf and gray matter in eeg simulations. *Brain Topography*, 16(4):245–248, 2004.

[34] A. Rienäcker, R. Beckmann, J. Pesch, G. Knoll, H. Buchner, and J. Silny. Dipolabbildung im FEM-Netz, Teil III: Berücksichtigung höherer Dipolmomente. Arbeitspapier zum Projekt Anatomische Abbildung elektrischer Aktivität des Zentralnervensystems, RWTH Aachen. November 1994.

[35] B. Roth, M. Balish, A. Gorbach, and S. Sato. How well does a three-sphere model predict positions of dipoles in a realistically shaped head. *Electroencephalography in Clinical Neurophysiology*, 87:175–184, 1993.

[36] M. Rullmann, A. Anwander, M. Dannhauer, S. Warfield, F. Duffy, and C. Wolters. Eeg source analysis of epileptiform activity using a 1 mm anisotropic hexahedra finite element head model. *NeuroImage*, 44(2):399–410, 2009.

[37] M. Rullmann, A. Anwander, S. Warfield, F. Duffy, and C. Wolters. EEG source analysis of epileptiform activity using a high resolution finite element head model. *NeuroImage*, 2008.

[38] S. Rush and D. Driscoll. Current distribution in the brain from surface electrodes. *Anesthesia and analgetica*, 47(6):717–723, 1968.

[39] J. Sarvas. Basic mathematical and electromagnetic concepts of the biomagnetic inverse problem. *Phys. Med. Biol.*, 32(1):11–22, 1987.

[40] R. Schmidt and G. Thews. *Physiologie des Menschen.* Springer-Verlag.

[41] N. Schmitz. *Vorlesungen über Wahrscheinlichkeitstheorie.* Teubner Verlag.

[42] R. Schönen, A. Rienäcker, R. Beckmann, and G. Knoll. Dipolabbildung im FEM-Netz, Teil I. Arbeitspapier zum Projekt Anatomische Abbildung elektrischer Aktivität des Zentralnervensystems, RWTH Aachen. 1994.

[43] K. Sekihara, S. Nagarajan, D. Poeppel, and A. Marantz. Performance of an meg adaptive-beamformer technique in the presence of correlated neural activities: Effects on signal intensity and time-course estimates. *IEEE Transactions on Biomedical Engineering*, 49(12):1534–1546, 2002.

[44] S. Silbernagl and A. Despopoulos. *Taschenatlas der Physiologie.* G. Thieme Verlag, 5th edition, 2001.

[45] R. Van Uitert and C. Johnson. Can a Spherical Model Substitute for a Realistic Head Model in Forward and Inverse MEG Simulations? In *Proceedings of the 13th International Conference on Biomagnetism*, August 2002.

[46] R. Van Uitert, D. Weinstein, and C. Johnson. Volume currents in forward and inverse magnetoencephalographic simulations using realistic head models. *Annals of Biomedical Engineering*, 31:21–31, 2003.

[47] S. Vallaghé, M. Clerc, and J.-M. Badier. In vivo conductivity estimation using somatosensory evoked potentials and cortical constraint on the source. In *4th IEEE Int. Symp. on Biomedical Imaging*, pages 1036–9, 2007.

[48] S. van den Broek, F. Reinders, M. Donderwinkel, and M. Peters. Volume conduction effects in eeg and meg. *Electroencephalography and Clinical Neurophysiology*, 106:522–534, 1998.

[49] B. Van Veen, W. van Drongelen, M. Yuchtman, and A. Suzuki. Localization of Brain Electrical Activity via Linearly Constrained Minimum Variance Spatial Filtering. *IEEE Transactions on Biomedical Engineering*, 44(9), 1997.

[50] J. Vrba and S. Robinson. Differences between Synthetic Aperture Magnetometry (SAM) and linear beamformers. In *J. Nenonen, R. Ilmoniemi, T. Katila, Editors. Biomag 2000: 12th International Conference on Biomagnetism. Espoo, Finland: Helsinki University of Technology*, pages 681–685, 2000.

[51] M. Wagner. *Rekonstruktion neuronaler Ströme aus bioelektrischen und biomagnetischen Messungen auf der aus MR-Bildern segmentierten Hirnrinde. Ph.D. thesis.* Shaker-Verlag Aachen, 1998.

[52] B. Widrow, K. Duvall, P. Gooch, and W. Newman. Signal cancellation phenomena in adaptive arrays: Causes and cures. *IEEE Trans. Antennas Propagat.*, 30:469–478, 1982.

[53] H. Wieringa. *MEG, EEG and the integration with magnetic resonace images.* Proefschrift Enschede.

[54] C. Wolters. *Direkte Methoden zur Berechnung dipolinduzierter elektrischer und magnetischer Felder und inverse Strategien zur Quellokalisation im Gehirn.* Diplomarbeit in Mathematik mit Nebenfach Medizin. Institut für Geometrische und Praktische Mathematik, RWTH Aachen, 1997.

[55] C. Wolters. *Influence of Tissue Conductivity Inhomogenity and Anisotropy on EEG/MEG based Source Localization in the Human Brain.* Number 39 in MPI Series in Cognitive Neuroscience. MPI of Cognitive Neuroscience Leipzig, 2003.

[56] C. Wolters, A. Anwander, G. Berti, and U. Hartmann. Geometry-adapted hexahedral meshes improve accuracy of finite element method based EEG source analysis. *IEEE Transactions on Biomedical Engineering*, 54(8):1446–1453, 2007.

[57] C. Wolters, A. Anwander, X. Tricoche, D. Weinstein, M. Koch, and R. MacLeod. Influence of tissue conductivity anisotropy on eeg/meg field and return current computation in a realistic head model: A simulation and visualization study using high-resolution finite element modeling. *NeuroImage*, 30:813–826, 2006.

[58] C. Wolters, L. Grasedyck, and W. Hackbusch. Efficient computation of lead field bases and influence matrix for the FEM-based EEG and MEG inverse problem. *Inverse Problems*, 20(4):1099–1116, 2004.

[59] C. Wolters, H. Köstler, C. Möller, J. Härtlein, L. Grasedyck, and W. Hackbusch. Numerical mathematics of the subtraction method for the modeling of a current dipole in EEG source reconstruction using finite element head models. *SIAM J. on Scientific Computing*, 30(1):724.

[60] Christoff Zalpour. *Für die Physiotherapie: Anatomie Physiologie*. Urban & Fischer, 1st edition, 2002.

Erklärung der Eigenständigkeit

Hiermit versichere ich, Stephanie Sillekens, dass ich die vorliegende Arbeit selbstständig verfasst und keine anderen als die angegebenen Hilfsmittel verwendet habe.
Gedanklich, inhaltlich oder wörtlich Übernommenes habe ich durch Angabe von Herkunft und Text oder Anmerkung belegt bzw. kenntlich gemacht. Dies gilt in gleicher Weise für Bilder, Tabellen und Skizzen, die nicht von mir selbst erstellt wurden.

Münster, 22.12.2008